Dalton Transactions

An international journal of inorganic chemistry

www.rsc.org/dalton

Volume 42 | Number 21 | 7 June 2013 | Pages 7485–7824

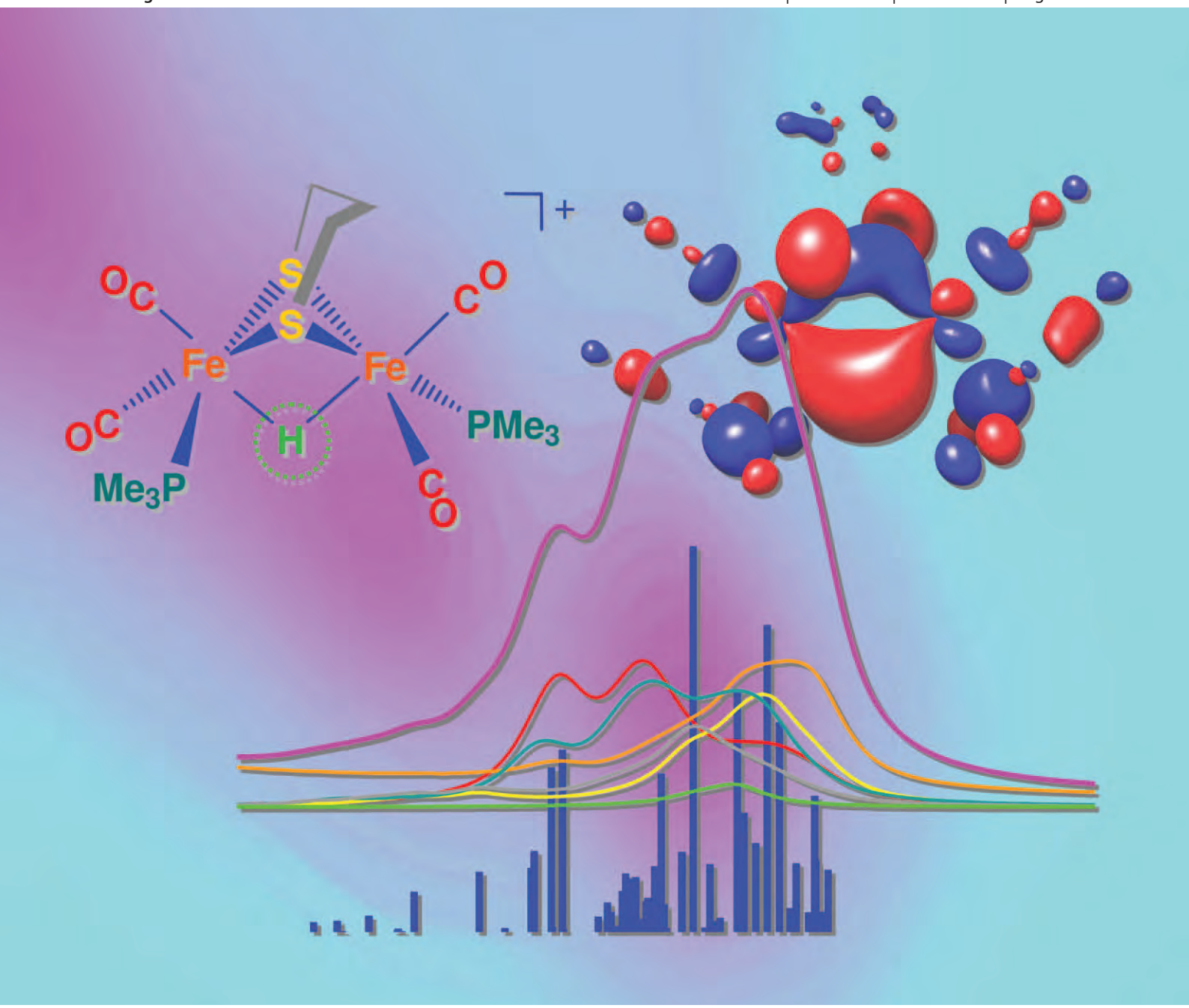

ISSN 1477-9226

RSC Publishing

COVER ARTICLE

Haumann *et al.*

Bridging-hydride influence on the electronic structure of an [FeFe] hydrogenase active-site model complex revealed by XAES-DFT

Dalton Transactions

RSC Publishing

PAPER

View Article Online
View Journal | View Issue

Cite this: *Dalton Trans.*, 2013, **42**, 7539

Bridging-hydride influence on the electronic structure of an [FeFe] hydrogenase active-site model complex revealed by XAES-DFT†

Nils Leidel,[a] Chung-Hung Hsieh,[b] Petko Chernev,[a] Kajsa G. V. Sigfridsson,‡[a] Marcetta Y. Darensbourg[b] and Michael Haumann*[a]

Two crystallized [FeFe] hydrogenase model complexes, **1** = (μ-pdt)[Fe(CO)$_2$(PMe$_3$)]$_2$ (pdt = SC1H$_2$C2H$_2$C3H$_2$S), and their bridging-hydride (Hy) derivative, **[1Hy]$^+$** = [(μ-H)(μ-pdt)[Fe(CO)$_2$ (PMe$_3$)]$_2$]$^+$ (BF$_4^-$), were studied by Fe K-edge X-ray absorption and emission spectroscopy, supported by density functional theory. Structural changes in **[1Hy]$^+$** compared to **1** involved small bond elongations (<0.03 Å) and more octahedral Fe geometries; the Fe–H bond at Fe1 (closer to pdt-C2) was ~0.03 Å longer than that at Fe2. Analyses of (1) pre-edge absorption spectra (core-to-valence transitions), (2) Kβ^{1,3}, Kβ′, and Kβ^{2,5} emission spectra (valence-to-core transitions), and (3) resonant inelastic X-ray scattering data (valence-to-valence transitions) for resonant and non-resonant excitation and respective spectral simulations indicated the following: (1) the mean Fe oxidation state was similar in both complexes, due to electron density transfer from the ligands to Hy in **[1Hy]$^+$**. Fe 1s→3d transitions remained at similar energies whereas delocalization of carbonyl AOs onto Fe and significant Hy-contributions to MOs caused an ~0.7 eV up-shift of Fe1s→(CO)s,p transitions in **[1Hy]$^+$**. Fed-levels were delocalized over Fe1 and Fe2 and degeneracies biased to O_h–Fe1 and C_{4v}–Fe2 states for **1**, but to O_h–Fe1,2 states for **[1Hy]$^+$**. (2) Electron-pairing of formal Fe(d^7) ions in low-spin states in both complexes and a higher effective spin count for **[1Hy]$^+$** were suggested by comparison with iron reference compounds. Electronic decays from Fe d and ligand s,p MOs and spectral contributions from Hys,p→1s transitions even revealed limited site-selectivity for detection of Fe1 or Fe2 in **[1Hy]$^+$**. The HOMO/LUMO energy gap for **1** was estimated as 3.0 ± 0.5 eV. (3) For **[1Hy]$^+$** compared to **1**, increased Fed ($x^2 - y^2$) – (z^2) energy differences (~0.5 eV to ~0.9 eV) and Fed→d transition energies (~2.9 eV to ~3.7 eV) were assigned. These results reveal the specific impact of Hy-binding on the electronic structure of diiron compounds and provide guidelines for a directed search of hydride species in hydrogenases.

Received 19th December 2012,
Accepted 11th February 2013

DOI: 10.1039/c3dt33042g

www.rsc.org/dalton

Introduction

Hydride species bound to transition-metal sites[1] play important roles in numerous areas of biological[2–4] and chemical[5–7] catalyses, H_2-storage technologies,[8–10] and present and future renewable energy applications for a hydrogen economy.[11–13] An improved understanding of the structural and, in particular, the electronic properties of hydride-binding in transition-metal compounds, therefore is expected to impact the development of improved tailored materials.[14]

In nature, dedicated metal complexes bound to protein molecules have evolved which catalyze reversible H_2-formation *via* metal-bound hydrides at very efficient rates. Prominent examples are hydrogenase enzymes, which contain iron and/or nickel atoms at their active sites.[15–17] In particular the so-called [FeFe] hydrogenases of bacteria and green algae are promising for (bio)technological applications[18] because of their superior H_2-production activity.[19–21] They contain a six-iron complex termed H-cluster (Fig. 1), which comprises a catalytically functional binuclear complex ($2Fe_H$) linked to a [4Fe4S] cubane cluster that is involved in electron transfer to $2Fe_H$.[22,23] The diiron sub-complex carries carbon monoxide (CO) and cyanide (CN^-) ligands[24,25] and a bridging dithiolate species, apparently being an azadithiolate (adt) group.[26,27] Limited information on the binding of O_2 to the diiron site of

[a]*Freie Universität Berlin, Institut für Experimentalphysik, 14195 Berlin, Germany. E-mail: michael.haumann@fu-berlin.de; Fax: +49 30 838 56299; Tel: +49 30 838 56101*

[b]*Texas A&M University, Department of Chemistry, Texas 77843, USA*

†Electronic supplementary information (ESI) available: (1) Crystallographic coordinates of **1** and **[1Hy]$^+$** (Table S1), (2) Kβ emission spectra of iron reference compounds for resonant excitation (Fig. S1), (3) Kβ CIE spectra for excitation at 7115.8 eV (Fig. S2). See DOI: 10.1039/c3dt33042g

‡Present address: MAX IV Laboratory, Lund University, 22100 Lund, Sweden.

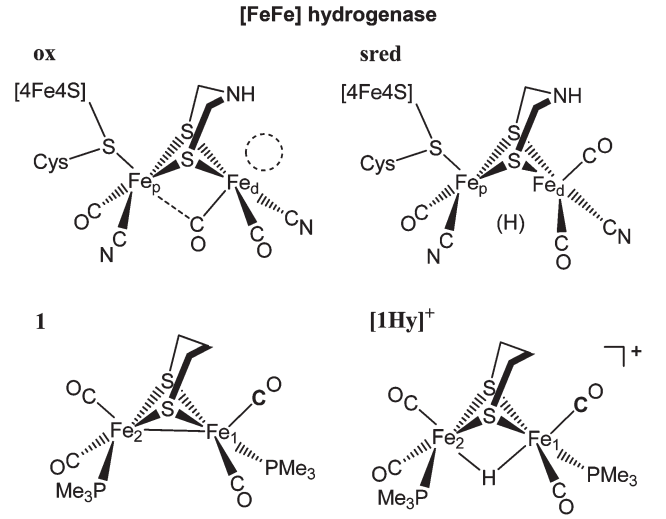

Fig. 1 Molecular structures of diiron sites in [FeFe] hydrogenase (top) and model complexes (bottom). For selected bond lengths and respective atomic coordinates in crystal structures of **1** (left) and **[1Hy]$^+$** holding a bridging hydride (right) see Tables 1 and S1.† The iron atom located closer to the central C-atom of the pdt ligand is denoted as Fe1. Putative structures for the diiron unit of the active-site H-cluster of [FeFe] hydrogenase in the oxidized (ox, left) and super-reduced (sred, right)[35] states were derived by modification of crystallographic data (PDB entry 3C8Y)[134] to include a nitrogen atom in the dithiolate bridge.[26] The dashed circle in the ox state denotes a ligand that may be a water species or absent;[23] [4Fe4S] denotes the cubane cluster unit and Cys a cysteine ligand from the protein. Rearrangement of the bridging CO ligand in the sred state is indicated by FTIR data and may be accompanied by binding of a hydrogen species (H) in a presently unknown position.[35]

[FeFe] hydrogenases has been obtained.[28–30] The most important aspect of the enzyme function, however, which is insufficiently understood, is the nature of H_2/H^+ reaction intermediates involving iron-hydride species. Improvement of the enzymes by protein engineering[31,32] and novel hydrogen catalysts may result from insights into the natural [FeFe] active site in comparison to synthetic hydride-bearing model complexes.

The presence of Fe–Fe bridging and/or terminal hydride species has been invoked in propositions for the H_2-catalysis mechanism of [FeFe] hydrogenases.[20,33,34] The H-cluster in its oxidized state may be formulated as (OC)(NC)Fe$_d$(μ-adt)(μ-CO)-Fe$_p$(CO)(CN)-[4Fe4S] (Fe$_d$ and Fe$_p$ denote the iron atoms in distal and proximal positions to the closest Fe of the [4Fe4S] unit), carrying a bridging CO ligand and an open coordination site at Fe$_d$.[25] Under reducing conditions, the bridging CO switches to a terminal Fe$_d$ ligand[25] and recently, on the basis of EPR results, it has been speculated that a hydride species then may become bound to iron in the super-reduced state (Fig. 1).[35] Further insights into the structures and electronic configurations of potential hydride states in the enzymes are required to discriminate bridging and terminal species.

In the last few decades, synthetic chemists have been very successful in preparing model complexes for the diiron site of [FeFe] hydrogenases.[36–46] A substantial fraction of this work has been devoted to complexes, (a) which contain iron-bound hydrides in metal-bridging and/or terminal positions, (b) that focus for example on the reactivity and redox potential of the compounds, (c) that explore the role of the dithiolate bridge in proton transfer, and (d) that demonstrate the influence of ligand exchange and coordination geometry at the iron atoms.[44,47–65] Unfortunately, the stabilities, turnover rates, and numbers of synthetic [FeFe] catalysts are thus far too low for technical applications. Furthermore, detailed information on the electronic configuration is available only for a limited number of complexes. The properties of hydride binding intermediates are of paramount interest, but difficult to study by spectroscopic methods. Novel approaches to characterize relationships between the molecular and electronic structures may aid the ongoing attempts to improve diiron complexes for H_2-catalysis applications.

In principle, a variety of experimental techniques is available for the physico-chemical characterization of metal-hydride compounds, including, for example, crystallography methods,[66] infrared,[67] Raman,[68] Mössbauer,[69] and photoelectron[70,71] spectroscopy, nuclear and electron magnetic resonance techniques,[72,73] and neutron scattering.[74] In combination with quantum chemical calculations, Raman spectroscopy has been used recently to assign vibrational frequencies of, *e.g.*, bridging and terminal Fe–H bonds.[75–78] Synchrotron-based X-ray absorption and emission spectroscopy (XAS, XES) and resonant inelastic X-ray scattering (RIXS) permit the study of all states of [FeFe] compounds in solid material and in solution.[79–83] By the combination of high-resolution XAS and narrow-band detection XES in a single experiment (XAES),[79,80,84–92] specific structural features (interatomic distances, site geometry, ligation patterns) and electronic properties (metal oxidation and spin states; molecular orbital energies, occupancies, and interactions) are derived, in an even spin- and site-selective fashion.[79,84,91–99] In particular, XAES has been employed to characterize iron compounds,[84,91–93,100–107] and the calculation of respective XAES spectra, *i.e.* emission and absorption lines due to valence-to-core transitions (*e.g.* Kβ^{2,5} emission) and core-to-valence transitions (*e.g.* pre-edge peaks of the metal K-edge) by density functional theory (DFT) methods is feasible.[84,91,92,100,102] The XAES-DFT approach has allowed, for example, assignment as a carbon of the central atom in the iron–molybdenum cofactor of nitrogenase,[108,109] determination of the electronic structure of industrial catalysts,[110] and site-selective determination of electronic parameters for the individual Fe ions[84] and discrimination of rotational isomers and iron-hydride intermediates in solution[91] for asymmetric [FeFe]-site models.

In the present study, XAES-DFT was employed to compare the electronic structures of two symmetric, crystallized diiron complexes, **1** = (μ-pdt)[Fe(CO)$_2$(PMe$_3$)]$_2$ (pdt = SCH$_2$CH$_2$CH$_2$S), and its bridging-hydride derivative, **[1Hy]$^+$** (BF$_4^-$) = [(μ-H)-(μ-pdt)[Fe(CO)$_2$(PMe$_3$)]$_2$]$^+$ (BF$_4^-$).[111] Specific spectral changes due to the hydride were well discernable in XAS pre-edge spectra (core-to-valence transitions), in XES Kβ spectra (valence-to-core transitions), and in respective RIXS data

(valence-to-valence transitions). Spectral analysis revealed the overall MO configurations and effective spin states, HOMO–LUMO energy gaps, and energy differences between unoccupied d-electron levels of iron, all of which was near-quantitatively corroborated by the DFT calculations. Herein is a comprehensive picture of the valence level energies and of the influence of the bridging hydride on the electronic configuration, in response to the structural alterations due to the hydride binding. Building on our previous XAES work on diiron compounds,[84,91,104] this study provides the methodology for the tracking of metal–hydride interactions in the reaction cycles of hydrogenase enzymes.

Materials and methods

Synthesis and sample preparation procedures

Complex **1** = (μ-pdt)[Fe(CO)$_2$(PMe$_3$)]$_2$ (pdt = SCH$_2$CH$_2$CH$_2$S) was prepared and crystallized as described earlier (see ref. 49 and 111 and references therein). Complex **[1Hy]$^+$** (BF_4^-) = [(μ-H)(μ-pdt)[Fe(CO)$_2$(PMe$_3$)]$_2$]$^+$ (BF_4^-)[49,111] was prepared by direct reaction of the diiron conjugate base with HBF_4. Powder material of **1** or **[1Hy]$^+$** was diluted by grounding with solid boron nitride and samples for the X-ray experiments were loaded into Kapton-covered acrylic-glass holders and frozen in liquid nitrogen until use.

X-ray experiments

X-ray spectroscopy was carried out at the undulator beamline ID26 of the European Synchrotron Radiation Facility (ESRF) at Grenoble (France).[84,91,104] Samples were held in a liquid-He cryostat at 20 K. The incident energy was set by an Si[311] double-crystal monochromator (energy bandwidth ~0.2 eV at the Fe K-edge). Iron XANES spectra were collected either in transmission mode or by monitoring the total X-ray fluorescence using a scintillation detector (~20 cm^2 area, placed at 90° to the incident X-ray beam and at ~1 m to the sample), which was shielded by a 10 μm Mn foil against scattered incident X-rays, using the rapid-scan mode of ID26. After signal averaging, XANES spectra were normalized to an edge jump of unity using the EXAFS region of the monochromator scan (not shown) and the pre-edge region was isolated by subtraction of a polynomial spline through the main edge rise. High energy-resolution emission detection was facilitated by a vertical-plane Rowland-circle spectrometer and a silicon-drift detector for monitoring the X-ray fluorescence. An energy bandwidth of ~1.0 eV at the Fe Kβ fluorescence lines was achieved using the [620] Bragg reflection of 5 spherically bent Ge wafers (R = 1000 mm). The energy axes of the monochromator and emission spectrometer were calibrated (accuracy ±0.1 eV) as outlined elsewhere.[84,91] For collection of RIXS plane data, the emission detection energy for XANES measurements was varied over the Kβ spectral region in 0.25–0.40 eV steps; RIXS data were averaged and evaluated using in-house Matlab (MathWorks) tools. For a schematic depiction of the set-up and further technical details of the X-ray experiments see ref. 84 and 91.

Density functional theory calculations

Spin-unrestricted single-point DFT calculations were performed with the program package ORCA[113] as previously.[84,91] The BP86 exchange correlation functional[114–116] and a triple-ξ valence plus polarization (TZVP+P) basis set[117] were used. Crystal structures of **1** and **[1Hy]$^+$** were used with a singlet ground state and an appropriate total charge of 0 (unprotonated) or 1+ (protonated at the Fe–Fe bond). The resulting MOs were visualized as isosurfaces with the programs Jmol or UCSF Chimera. The contributions of individual Fe-d atomic orbitals to the MOs were determined from calculations on appropriately oriented model structures,[84,91] using Mulliken population analysis.[118] X-ray absorption K-edge intensities in the pre-edge region (core-to-valence transitions) were calculated using a time-dependent DFT (TD-DFT) formalism[101,102] and Kβ valence-to-core transitions (Kβ^{2,5} emission) were calculated using the DFT approach described in ref. 100 and 106 (see also ref. 84 and 91). A spin multiplicity of M = 1 was employed in both calculation procedures. A shift to higher energies by 181.35 eV and, if not otherwise stated, 1.0 eV Lorentzian broadening of stick spectra were applied to calculated Kβ emission lines and pre-edge absorption spectra for comparison with the experimental data. For further computational details see ref. 84 and 91.

Results

FeFe model complex synthesis and crystal structures

Two diiron-carbonyl compounds, **1** and **[1Hy]$^+$** (Fig. 1), were synthesized following previously established procedures. (μ-pdt)[Fe(CO)$_2$(PMe$_3$)]$_2$ (pdt = SCH$_2$CH$_2$CH$_2$S), further on denoted **1**, was prepared and crystallized as outlined in ref. 111, reproducing the previously reported structural parameters. A derivative of **1**, [(μ-H)(μ-pdt)[Fe(CO)$_2$(PMe$_3$)]$_2$]$^+$, henceforth denoted **[1Hy]$^+$**, was prepared by direct reaction of the diiron conjugate base with HBF_4, resulting in protonation of the iron–iron bond to produce a formal bridging hydride. The crystal structure of the BF_4^- salt of **[1Hy]$^+$** was very similar to that of the PF_6^- salt of the same hydride compound,[111] showing statistically non-significant differences in bond lengths. Respective atomic coordinates are summarized in the ESI (Table S1†). The main structural effects of the Fe–Fe bond protonation in **[1Hy]$^+$** were minor elongations of the iron–ligand bonds, by ~0.01 Å on the average, and an ~0.03 Å larger Fe–Fe distance. Slight positional changes of the CO and PMe$_3$ ligands resulted in more regular octahedral (O_h) geometries at both iron atoms, as compared to the distorted square-pyramidal (C_{4v}) iron atoms in **1**. The two Fe–H bonds in **[1Hy]$^+$** differ by as much as ~0.03 Å (Table 1). This emphasizes the inherent asymmetry in **[1Hy]$^+$** (and **1**) due to the orientation of the central C-atom of the μ-pdt group towards Fe1 (Fig. 1). Thus, the two iron atoms in principle were distinguishable in the powder samples of **1** and **[1Hy]$^+$** used for the XAES experiments.

Table 1 Bond lengths in crystal structures of **1** and **[1Hy]$^+$**. For the mean iron–ligand distances, values in parentheses represent the full range of bond length variations in the structures (Fig. 1)

	1	**[1Hy]$^+$**	**[1Hy]$^+$ − 1**
	Mean distance, R [Å]		ΔR [Å]
Fe1–H	—	1.693	—
Fe2–H	—	1.659	—
Fe1–C(O)	1.758(3)	1.777(17)	0.019
Fe2–C(O)	1.758(9)	1.770(9)	0.012
Fe1–P(Me_3)	2.235	2.251	0.016
Fe2–P(Me_3)	2.234	2.237	0.003
Fe1–S	2.253(6)	2.265(3)	0.012
Fe2–S	2.253(6)	2.262(1)	0.009
Fe–Fe	2.555	2.580	0.025
Fe1(C)═O	2.914(2)	2.915(14)	0.001
Fe2(C)═O	2.915(3)	2.913(10)	−0.002

Configurations of valence orbitals of iron from DFT

Single-point DFT calculations at the BP86/TZVP theory level on the electronic configuration of **1** and **[1Hy]$^+$** were performed using the crystal structures and assuming a low-spin (l.s.) ground state with unity spin multiplicity ($M = 2S + 1$) in both cases, *i.e.* two electrons from each of the formal $Fe^I(3d^7)$ ions are paired. The latter was experimentally revealed by the XAES results described in the next section. For both **1** and **[1Hy]$^+$**, the calculated MOs with predominant Fed character in general were strongly delocalized over both Fe ions (Fig. 2). The respective MO energies and occupancies translated into apparent d-orbital degeneracies in an atomic level representation, which differed between the two iron atoms and between **1** and **[1Hy]$^+$** (Fig. 2). For both complexes, the Fed_{z^2} orbital is pointed along the axis defined by the apical CO ligands and the vacant coordination site in **1** or the bridging hydride in **[1Hy]$^+$**. In tendency, in **1** the d-level degeneracy for Fe1 more closely resembled a l.s. O_hFe^{II} ion with unoccupied $Fed_{x^2-y^2}$ and Fed_{z^2} orbitals whereas Fe2 more closely resembled a l.s. $C_{4v}Fe^0$ ion with an occupied Fed_{z^2} orbital at lower energy. This reflects considerable electronic asymmetry at the two iron atoms. The HOMO and LUMO in **1** showed predominant Fed_{z^2} character with an apparent energy gap of 2.5 eV. The HOMO reflected Fe–Fe bonding and showed Fe1 and Fe2 contributions of 21.2% and 27.4%. Two electrons from the formal Fe^I ions pair in an MO with mixed Fed character (Fig. 2).

Compared to **1**, for **[1Hy]$^+$** lower energies, by ~0.4 eV, of all MOs reflect the surplus positive charge, the electronic asymmetry was lessened, and the d-level degeneracies of both Fe ions more closely resembled l.s. O_hFe^{II} species. However, the Mulliken charges on the Fe ions of **[1Hy]$^+$** were calculated to be close to zero and therefore by a mean value of ~0.15 units more negative than for **1** (Table 2). The hydride carried a charge of only about −0.06 units. This is by ~0.28 units more negative than the average charge of the remaining protons in the complex, thus reflecting significant charge transfer onto the μ-H bridge, mainly from the non-Fe atoms. For **[1Hy]$^+$** the LUMO still displayed Fed_{z^2} character, but now the Fe–Fe antibonding HOMO at an energy of −8.69 eV was dominated by

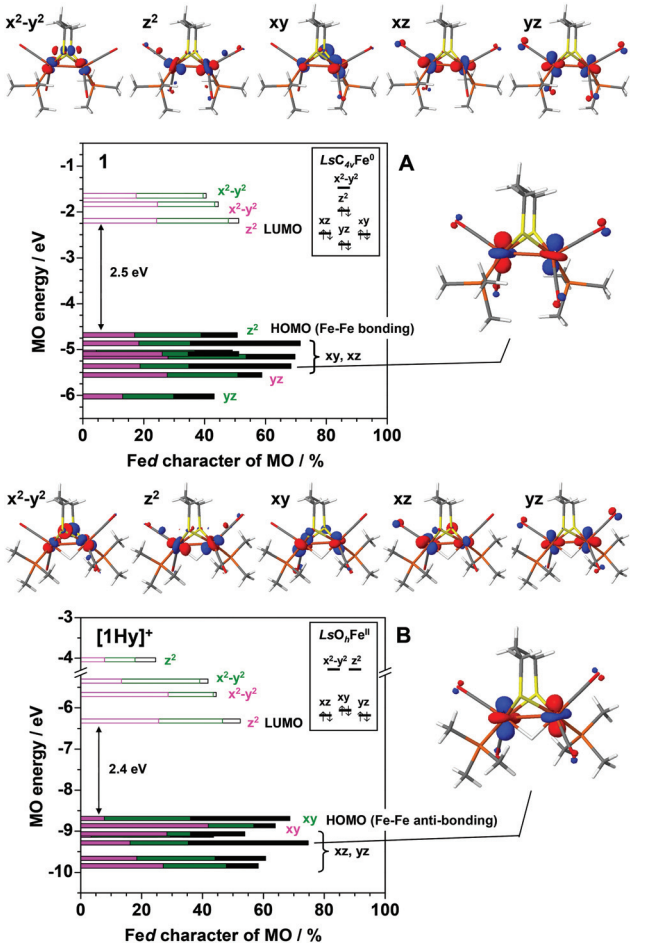

Fig. 2 Energies, Fed-AO contributions, and shapes of MOs from DFT calculations. Values were derived for crystal structures of **1** (A) and **[1Hy]$^+$** (B) at the BP86/TZVP level of theory. Bar energies give average values for spin-up and spin-down MOs. Solid bars, occupied MOs; open bars, empty MOs; magenta (Fe1) and green (Fe2) bars denote contributions from the indicated Fed AOs to the total sum (black bars). Energies are for consecutive MOs, except for the highest-energy MO of **[1Hy]$^+$**, which is the 9th one after the shown MO with the 2nd-highest energy. Calculated HOMO–LUMO energy gaps and HOMO character are indicated. The insets show idealized Fed AO degeneracies in an atomic-level description. Graphs on top of (A) and (B) show MO shapes for the largest indicated Fed AO contributions. Graphs on the right represent MOs proposed to contain the paired d-electrons of the two formal $Fe^I(d^7)$ ions.

Table 2 Mulliken charges from DFT for crystal structures

	1	**[1Hy]$^+$**	**[1Hy]$^+$ − 1**
	Mulliken charge, C_M		ΔC_M
Fe1	0.13	−0.02	−0.15
Fe2	0.16	−0.01	−0.17
Hy	—	−0.06	—
CO	−0.86	−0.23	0.63
PMe_3	0.64	1.11	0.47
S	−0.16	−0.02	0.14
pdt[a]	0.09	0.23	0.14
Sum	0	1	1

Hy = bridging hydride. Given values represent the sum over the respective atoms or groups. [a] The bridging ligand without the S-atoms is denoted pdt.

Fed$_{xy}$ contributions mostly from Fe2, showing total Fe1/Fe2 contributions of 20.1/46.2%. The HOMO–LUMO gap was reduced to 2.4 eV, and two electrons from the Fe ions seemingly pair in an MO with an altered Fed$_{xz,yz}$ mixture (Fig. 2).

Fe XANES spectra and core-to-valence transitions

XANES spectra of **1** and **[1Hy]**$^+$ were collected to study electronic transitions from the 1s core level to bound unoccupied valence states (Fig. 3). The main edge energies (at 50% level) of both complexes were similar (~7122.5 eV) and therefore the apparent mean oxidation state of the Fe ions was similar (Fig. 3A), in agreement with the calculated Mulliken charges (Table 2). The steeper edge slope for **[1Hy]**$^+$ was attributable to the increased symmetry at its Fe ions due to the hydride binding. The pre-edge features in the XANES exhibited two main maxima (Fig. 3A, inset), with the 1st maximum being at similar energies for both complexes, again suggesting a similar Fe oxidation state. The 2nd maximum was at higher energies by ~1.7 eV for **1**, but by ~2.2 eV for **[1Hy]**$^+$ (Table 3).

Time-dependent DFT calculations revealed the electronic transitions that accounted for the pre-edge absorption (Fig. 3B). The pre-edge spectra that were obtained based on the calculated transition intensities reproduced the experimental spectra quite well for both complexes, in particular the relative intensities of the two peaks and the increased energy difference between peaks 1 and 2 for **[1Hy]**$^+$ compared to **1** (Table 3). The 1st pre-edge peak was dominated by 1s→Fed$_{z^2}$ and 1s→Fed$_{x^2-y^2}$ transitions, with the former transitions into the LUMO being at the lowest energies, and this peak thus can be considered as a true 1s→3d feature.[119] The second peak is not a pre-edge feature in the narrow sense, because it mostly reflects transitions from the 1s level into MOs with predominant (>55%) s,p-character of the (CO) ligands. For **1**, these transitions occurred mainly into (CO)s,p MOs, which were quite localized at Fe1 or Fe2, for excitation of either Fe1 or Fe2. In contrast, the respective (CO)s,p MOs were more delocalized over both Fe ions for **[1Hy]**$^+$. For **[1Hy**$^+$**]**, the hydride contributed significantly (~10%) to the transitions at the highest energies of the second pre-edge feature (Fig. 3B). Therefore, energy up-shifts of more delocalized (CO)s,p-dominated MOs and hydride contributions accounted for the higher energy of the second pre-edge feature in the experimental XAS spectrum of **[1Hy]**$^+$.

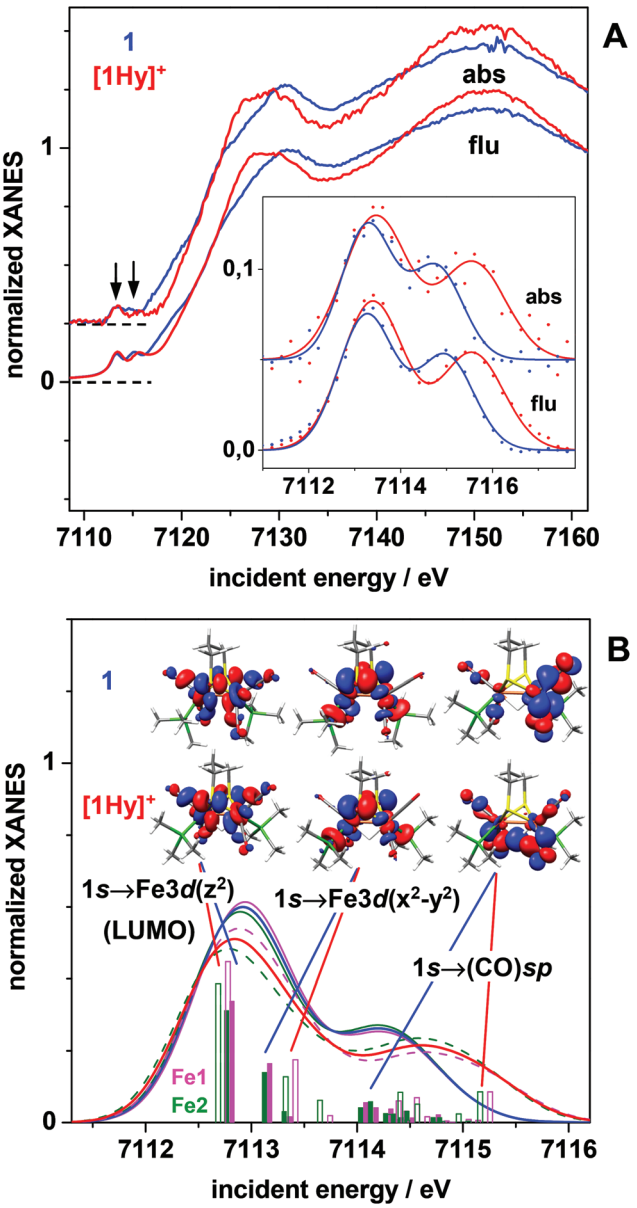

Fig. 3 Iron pre-edge spectra from XANES and DFT due to core-to-valence transitions. (A) Experimental Fe K-edge spectra and (arrows) isolated pre-edge features in the inset for X-ray absorption (abs) or total-fluorescence (flu) detection. Curves in the inset represent fits to the data points by two Gaussians with (mean) parameters in Table 3. (B) DFT-calculated energies and intensities of electronic transitions at the pre-edge (bars: solid, **1**; open, **[1Hy]**$^+$; magenta/green, excitation of Fe1 or Fe2; dominant AO contributions from Fe or (CO)-ligands to the MOs shown on top are indicated. Lines were obtained by 1 eV Lorentzian broadening of stick spectra (black, sum of spectra for Fe1 (magenta) and Fe2 (green)); for peak energies and areas see Table 3.

Kβ XES spectra and valence-to-core transitions

X-ray emission spectra in the Kβ region were collected to study electronic decay processes from occupied levels (Fe3p, valence states) to the 1s core hole (Fig. 4). For non-resonant excitation into the continuum using an energy of 7600 eV well above the iron K-edge, the Kβ main line (Kβ^{1,3}, Kβ′) spectra due to Fe 3p→1s decay processes revealed overall similar shapes for **1** and **[1Hy]**$^+$ and a slight shift of spectral intensity to lower energies for **[1Hy]**$^+$ (Fig. 4A). The small amplitude of the Kβ′ feature of both complexes is typical for low-spin transition metal complexes carrying no unpaired electrons.[79,96,120] The Kβ′ emission is a spin-polarization feature mostly explained by Fe(3p,3d) exchange coupling between unpaired metal 3d spin-up (or spin-down) electrons and a spin-up (or spin down) hole in the 3p level in the final state.[98,121–123] The Kβ′ intensity thus decreases with decreasing numbers of unpaired 3d electrons, *i.e.* with the spin state.[79,96,99,120] This showed that two electrons of the formal Fe^{I}(d^7) ions were paired (spin multiplicity of 1), *i.e.* unpaired electrons were absent, as used in the DFT

Table 3 Peak areas (A) and energies (B) of XAS pre-edge and XES Kβ^{2,5} spectra

	1		**[1Hy]$^+$**		**[1Hy]$^+$ − 1**	
	A [r.u.]	E-7100 [eV]	A [r.u.]	E-7100 [eV]	Δ*A* [r.u.]	Δ*E* [eV]
	exp. (DFT)[b]					
XAS pre-edge	0.11 (0.12)	13.3 (13.3)	0.15 (0.16)	13.5 (13.4)	0.03 (0.04)	0.2 (0.1)
	0.07 (0.06)	14.9 (15.0)	0.09 (0.08)	15.6 (15.7)	0.03 (0.02)	0.7 (0.7)
	−0.04[a] (−0.06)[a]	1.6[a] (1.7)[a]	−0.06[a] (−0.08)[a]	2.1[a] (2.3)[a]	0[a] (−0.02)[a]	0.5[a] (0.6)[a]
XES Kβ^{2,5}	1.7 (1.2)	−5.0 (−5.0)	1.6 (1.3)	−5.4 (−5.1)	−0.1 (0.1)	0.4 (0.1)
	3.3 (4.3)	0 (0)	3.4 (3.9)	0.2 (0.3)	0.1 (−0.4)	0.2 (0.3)
	6.1 (6.1)	4.1 (4.1)	6.1 (6.5)	4.2 (4.2)	0 (0.4)	0.1 (0.1)
	5.0 (4.9)	7.6 (7.8)	6.0 (7.1)	7.6 (7.7)	1.0 (2.2)	0 (−0.1)
	4.8 (4.3)	10.3 (10.6)	5.0 (3.3)	10.0 (10.5)	0.2 (−1.0)	−0.3 (−0.1)

Values were derived from fits using 2 (pre-edge; FWHM of 1.3 eV for **1** and 1.6 eV for **[1Hy]$^+$**) or 5 (Kβ^{2,5}; FWHM of 3.5 eV) Gaussians to experimental spectra in Fig. 3A (inset) and 4B (non-resonant excitation) and to DFT-calculated spectra in Fig. 3B and 5 (black sum spectra). Experimental parameters from XAS are mean values for absorption- and fluorescence-detected spectra. [a] Differences between values in the vertical direction of the table. [b] The energy axes for values from DFT were scaled by a factor of 1.25 and the summed amplitudes were normalized to the experimental data for comparison with the experimental data.

calculations. Indeed, the intensity of the Kβ′ feature for both complexes was located close to the zero position on the straight line, which accounts, in the case of non-resonant excitation, for the relation between the number of spin–spin interactions and the Kβ′ intensity for a series of iron complexes with increasing numbers of unpaired electrons[84] (Fig. 4A, see the legend).

A quite different picture was obtained for resonant excitation into the two pre-edge features (Fig. 4B). Excitation into the first pre-edge feature (7113.4 eV), initiating 1s→3d$_{z^2,x^2-y^2}$ transitions, resulted in an about doubled intensity of the Kβ′ emission. In this case, a surplus unpaired spin-up (or spin down) electron in the Fed levels and a spin-up (or spin down) 3p hole were expected in the Fe3d^{n+1}3p^5 final state. Comparison with the Kβ′ intensities of spectra (ESI, Fig. S1†), obtained by a similar resonant 1s→3d excitation of a series of iron complexes with increasing spin state, revealed that the Kβ′ intensity for **1** and **[1Hy]$^+$** indeed was in agreement with the presence of a single unpaired electron (Fig. 4B, see the legend). However, the slope of the line, describing the correlation between the Kβ′ intensity and the number of spin–spin interactions for resonant excitation, was about 4 times larger than the one for non-resonant excitation (Fig. 4B, inset). Accordingly, resonant excitation into Fed levels enables considerably more sensitive counting of unpaired electrons and spin state determination.

For excitation into the second pre-edge feature (7115.8 eV), initiating mostly 1s→(CO)s,p transitions, the Kβ′ feature was smaller compared to the 1s→3d case, but larger than for non-resonant excitation (Fig. 4A). Presumably, this is explained by the decreased coupling between the 3p hole and the surplus electron in the ligand-s,p levels at higher energies. This observation suggests that the Kβ′ feature probes an effective spin state, *e.g.* depending on the energy level and coupling strength of the unpaired electron, rather than the absolute (calculated) number of unpaired spins. This view seemingly was corroborated by the slightly higher Kβ′ intensity for **1** compared to **[1Hy]$^+$** as revealed in the respective difference spectrum (Fig. 4A), because for **1** the apparent Fed-level configuration (Fig. 3B) could account for a higher effective mean spin state.

Emission spectra in the Kβ^{2,5} region were collected, which reflect electronic decay processes from valence levels to the 1s hole (valence-to-core transitions) (Fig. 4B). The summed Kβ^{2,5} intensities for both complexes are located well on the line that accounts for the relation between the Kβ^{2,5} intensity and the mean Fe–ligand bond length in a series of iron complexes[84] (Fig. 4B, inset). For non-resonant excitation, the Kβ^{2,5} spectra showed five main peak features (a–e, Table 3) and in particular, significant higher intensities of peaks (c) and (d) and lower intensity of peak (e) were observed for **[1Hy]$^+$**. This suggested considerable hydride contributions to the Kβ^{2,5} spectrum of **[1Hy]$^+$**, as quantified by the DFT calculations described further below.

Resonant excitation resulted in an increased resolution of the five peak features in the Kβ^{2,5} lines, due to the diminished influence of lifetime broadening effects,[105,124] and in the enhancement of spectral differences between **1** and **[1Hy]$^+$** (Fig. 4B). For excitation into the first pre-edge feature (1s→3d$_{z^2,x^2-y^2}$ transitions), the emission peak (d) showed the highest intensity for both complexes and intensity mainly was gained in the region of peak (c) for **[1Hy]$^+$** compared to **1**. For excitation into the second pre-edge feature (1s→(CO)s,p transitions), peak (c) showed the highest intensity for both complexes and intensity mainly was gained in the region of peak (d) for **[1Hy]$^+$**. For both excitation energies, peak (e) was almost absent for **[1Hy]$^+$**. These spectral changes are consistently explained by the DFT calculations described in the next section.

DFT calculation of Kβ^{2,5} emission lines

The spectral shapes of the Kβ^{2,5} lines that resulted from broadening of the stick spectra, as calculated for both complexes using DFT, are shown in Fig. 5. They almost quantitatively

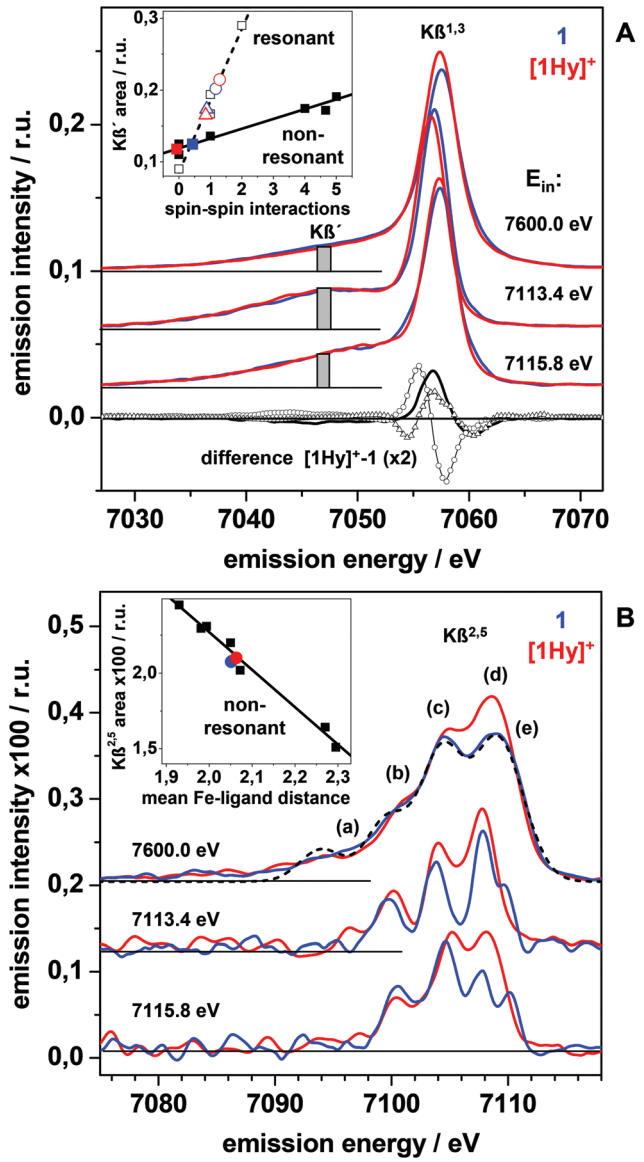

Fig. 4 Iron XES spectra in the Kβ emission region. (A) Spectra in the $K\beta^{1,3}$ and Kβ′ energy range (Fe 3p→1s transitions) for non-resonant (7600 eV) and resonant excitation at incident energies (E_{in}) centered at the first (7113.4 eV) or second (7115.8 eV) pre-edge peak of the XANES (compare Fig. 3A). Spectra were normalized to unity total area in the whole Kβ region and vertically displaced for comparison. Grey bars emphasize Kβ′ intensity differences. Difference spectra: black line, 7600 eV; open circles, 7113.4 eV; open triangles, 7115.8 eV. The inset shows Kβ′ intensities (for 7038–7048 eV integration of spectral areas) for **1** and **[1Hy]$^+$** and iron reference compounds (see ref. 84 and 91 for respective structures and Kβ spectra) for non-resonant excitation at 7600 eV (solid squares, for increasing Kβ′ area: $Fe^{II}S_2$, $Fe^0{}_2(CO)_9$, $Fe^{III}(dedtc)_3$ (dedtc = diethyldithiocarbamate), $Fe^{II}O$, $Fe^{II}Fe^{III}{}_2O_4$, $Fe^{III}{}_2O_3$) or resonant excitation into the 1st pre-edge peak (open squares; for increasing Kβ′ area: $Fe^{II}Fe^{III}{}_2O_4$, $Fe^0{}_2(CO)_9$, $[Cl_2bdtFe^I{}_2(CO)_4(Ph_2P–CH_2–NCH_3–CH_2–PPh_2)]$ (bdt = benzene-1,2-dithiolate), $Fe^{III}(dedtc)_3$ (see ESI, Fig. S1† for respective Kβ spectra and ref. 84 for structures) and linear regression lines. (B) $K\beta^{2,5}$ emission lines (valence-to-core transitions) for the same measuring conditions as in (A). The inset shows $K\beta^{2,5}$ intensities (for 7085–7115 eV integration) of reference compounds (squares, for increasing Fe–ligand distance; see also ref. 84): $Fe^0{}_2(CO)_9$, $Fe^{II}(CN)_6$, $Fe^I{}_2S_2(CO)_6$, $Fe^{II}{}_2(cp)_2(CO)_4$, $[Fe^I{}_2(\mu\text{-adt–}CH_2–Ph)(CO)_4(PMe_3)_2]$ (adt = S–CH_2–NBz–CH_2–S), $Fe^{II}S_2$, $Fe^{III}(dedtc)_3$; and a linear regression line. The origin of line features denoted a–e is discussed in the text. For energies and areas of emission lines in (B) see Table 3. The dashed line in (B) shows the DFT-calculated $K\beta^{2,5}$ spectrum of **1** after application of a scaling factor of 1.25 to its energy axis.

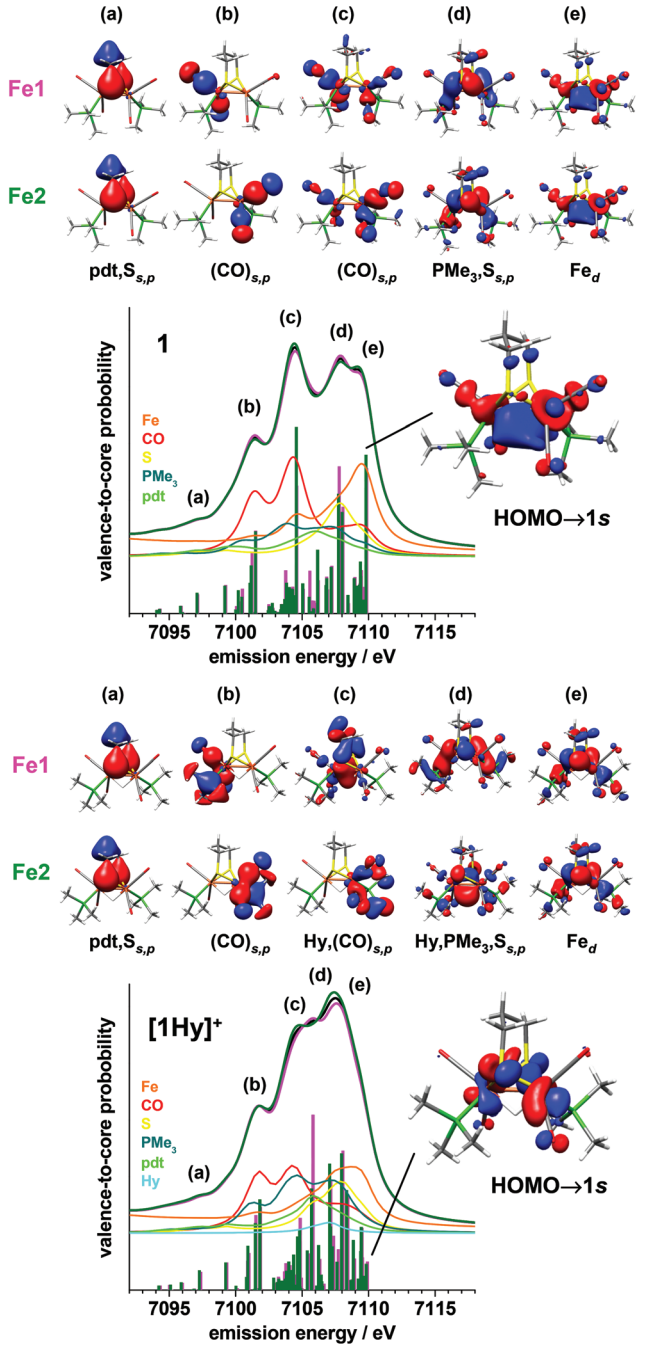

Fig. 5 DFT calculations of $K\beta^{2,5}$ valence-to-core transitions. Calculated transition energies and intensities (sticks; magenta/green, Fe1/2 transitions) and line spectra for 1 eV Lorentzian broadening (black lines, mean of spectra for Fe1 and Fe2; for peak areas and energies see Table 3) are displayed together with the line spectra for the indicated AO contributions to the electronic transitions (see colour code). The bridging ligand without the S-atoms is denoted pdt. Graphs on top show MO shapes and dominant AO contributions for transitions with highest intensities in the spectral regions a–e. Graphs on the right show the HOMO; note the pronounced intensity difference of HOMO→1s transitions for **1** and **[1Hy]$^+$**.

reproduced the main features (*i.e.* five maxima, Table 3) of the experimental spectra (compare Fig. 4B). Examination of the occupied MOs, the decay from which accounted for most of

the intensity (largest stick) of the peak features (a–e), revealed that for both complexes, peak (a) was dominated by decay from MOs with (pdt,S)s,p character and peak (b) mostly reflected decay from MOs with (CO)s,p character. Peaks (c) and (d) were due to decays from MOs with dominant (CO)s,p and ((PMe$_3$),S)s,p character. For **[1Hy]$^+$**, peak (c) for excitation of Fe1 and peak (d) for excitation of Fe2 in addition revealed significant hydride contributions. Accordingly, the pronouncedly increased intensity around peaks (c) and (d) in the experimental K$\beta^{2,5}$ spectrum of **[1Hy]$^+$** reflected specifically the hydride binding.

High oscillator strength of decay from the HOMO, showing mostly Fed$_{z^2}$ character, accounted for peak (e) in the calculated spectrum of **1**. The pronouncedly reduced amplitude of this peak for **[1Hy]$^+$** was attributable to a largely diminished intensity (to <20%) of the HOMO→1s decay, but the transition was calculated to be even at ~0.05 eV higher energy in **[1Hy]$^+$**. A similarly decreased peak (e) was observed in the experimental K$\beta^{2,5}$ spectra of **[1Hy]$^+$**, best visible for resonant excitation (Fig. 4B), and thus attributed to the diminished HOMO→1s contribution. Accordingly, only for **1** could a reasonable estimate of the HOMO–LUMO energy gap from the energy of peak (e) in the K$\beta^{2,5}$ spectrum (Fed$_{z^2}^{HOMO}$→1s decay) and from the energy of the first pre-edge peak (1s→Fed$_{z^2}^{LUMO}$ excitation) from the experimental data (Table 3) of 3.0 ± 0.5 eV be obtained. This value is in good agreement with the value of ~3.1 eV that was calculated on the basis of the DFT result (Fig. 2; Table 3; see the legend for calculation details).

Comparison of the experimental K$\beta^{2,5}$ spectra for resonant excitation (Fig. 4B) and the calculated lines (Fig. 5) revealed that for 1s→Fe3d (1st pre-edge peak) or 1s→(CO)s,p excitation (2nd pre-edge peak) the (PMe$_3$),Ss,p→1s or (CO)s,p→1s features were maximal for both complexes. In other words, a surplus electron in the Fe3d or (CO)s,p levels enhanced decays from the (PMe$_3$),Ss,p or (CO)s,p levels, at the expense of the respective complementary levels. In the calculated spectra, overall rather small spectral differences were observed for decay into the 1s holes on either Fe1 or Fe2. However, hole refilling on Fe1 or Fe2 occurred from (CO)s,p dominated MOs, which were quite localized on the respective (CO) ligands of either ion, in particular for **1**. For **[1Hy]$^+$**, an increased degree of delocalization of (CO)s,p MOs was observed. For **1**, peak (c) mainly reflected decay from (CO)s,p MOs of Fe2 and peak (d) from (PMe$_3$),Ss,p MOs of Fe1, whereas for **[1Hy]$^+$** this was reversed. This suggested a limited degree of site-selectivity in the spectra, *i.e.* monitoring preferentially of either Fe1 or Fe2 at selected emission energies.[84,91–93] A closer inspection of experimental and calculated K$\beta^{2,5}$ difference spectra (**[1Hy]$^+$ − 1**) corroborated this notion (Fig. 6). Apparently, the difference spectrum calculated for Fe1 more closely resembled the experimental spectrum for 1s→Fe3d excitation, meaning that a surplus Fed electron enhanced (CO)s,p→1s transitions, and the difference spectrum calculated for Fe2 was better in agreement with the experimental spectrum for 1s→(CO)s,p excitation, *i.e.* a surplus (CO)s,p electron enhanced (PMe$_3$),Ss,p→1s transitions, for **[1Hy]$^+$**.

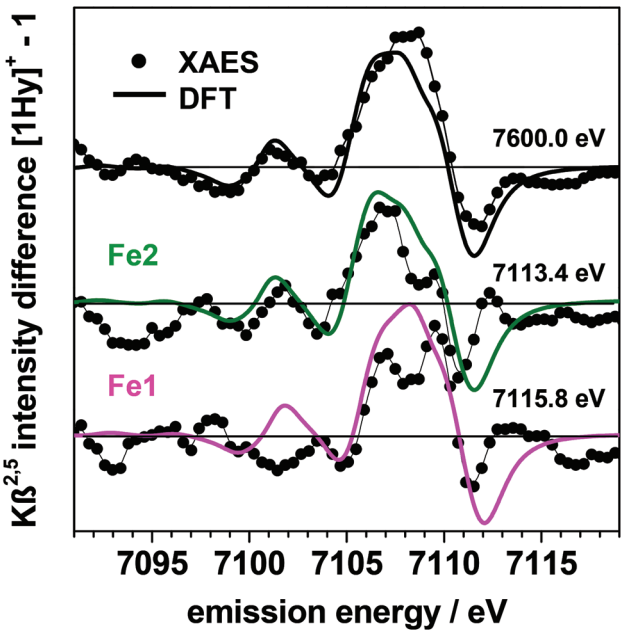

Fig. 6 Comparison of experimental and DFT-calculated K$\beta^{2,5}$ spectral differences (**[1Hy]$^+$ − 1**). Dots, experimental data (compare Fig. 4B); lines, DFT calculations (compare Fig. 5); spectra were vertically shifted. Experimental spectra are for three excitation energies, calculated spectra are for non-resonant excitation (top, average of spectra for Fe1 and Fe2; middle, Fe2; bottom, Fe1). The energy axes of calculated spectra were scaled by a factor of 1.25 and spectra were realigned with the experimental data for comparison.

RIXS studies in the Kβ emission regions

By variation of the excitation energy and of the emission detection energy in an RIXS experiment in the Kβ region, the energies of initial, intermediate, and final states are obtained.[79,80] In principle, this permits access to electronic transitions using high-energy K-edge excitation, for example metal p,d→d, metalp,d→ligands,p, ligands,p→metald, and ligand s,p→s,p transitions, which otherwise can only be initiated using low X-ray energies at the metal M-edge or even UV/vis light for excitation[125] (Fig. 7).

Contour plots of emission intensities for excitation in the pre-edge region of the Fe K-edge and emission detection in the K$\beta^{1,3}$/Kβ' and K$\beta^{2,5}$ regions (RIXS plane data) for **1** and **[1Hy]$^+$** overall appeared to be rather similar for the two complexes (Fig. 8). However, transects through the RIXS planes for constant incident energy (CIE) or constant final state energy (CFE) revealed more subtle spectral differences (Fig. 9).

CIE line plots in the 1st pre-edge peak region for K$\beta^{1,3}$ emission detection in principle correspond to M-edge spectra due to Fe 3p→3d excitations (Fig. 9A). Fits of the K$\beta^{1,3}$ CIE and CFE spectra using two Lorentzians revealed an ~0.4 eV larger energy difference between the two lines in the case of **[1Hy]$^+$** compared to **1** (Table 4), due to a more pronounced shift of the second line to higher energies in **[1Hy]$^+$**. The DFT calculations have yielded an ~0.4 eV increased energy difference between the 1s→3d$_{z^2}$ and 1s→3d$_{x^2-y^2}$ transitions for **[1Hy]$^+$**, due to a larger energy up-shift of the latter transitions

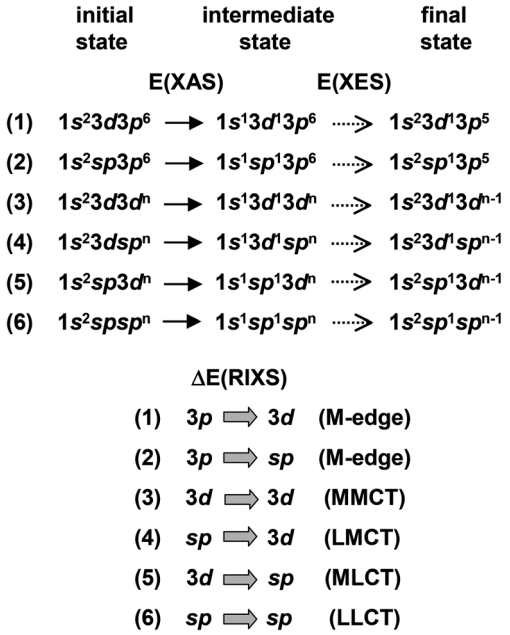

Fig. 7 Overview of electronic transitions in resonant-excitation XAS, XES, and RIXS. Shown are transitions between metal-d and ligand-s,p electronic states in an atomic level description. The energy differences, Δ*E*, derived from RIXS data (bottom) result from the differences of excitation, *E*(XAS), minus emission, *E*(XES), energies (top). Respective energy differences here were obtained using hard X-rays at the Fe K-edge and otherwise may be determined by low-energy M-edge or UV/vis spectroscopy of metal/ligand charge transfer processes (M/LCT).

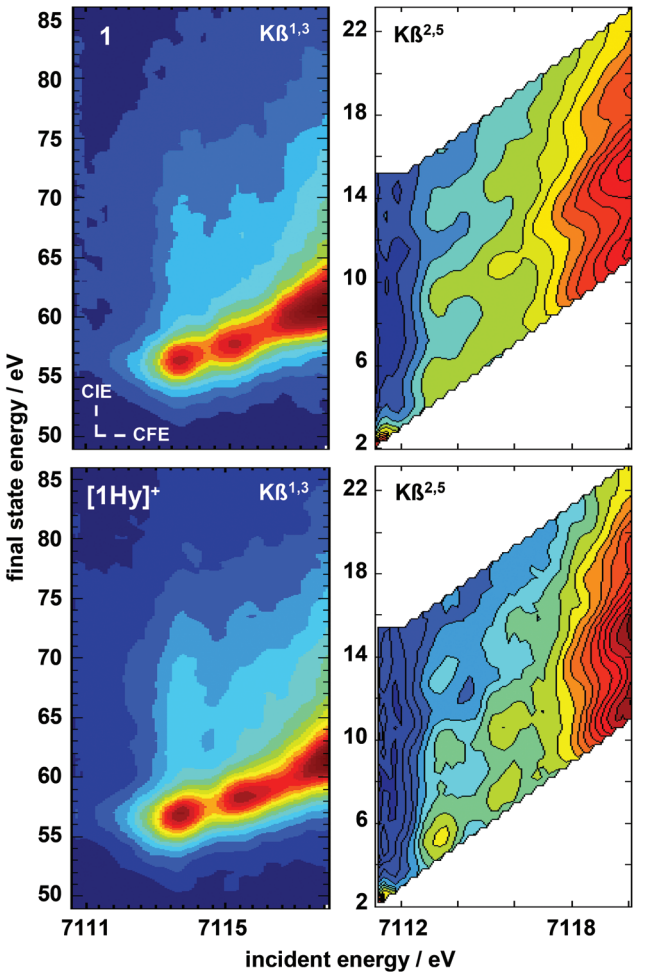

Fig. 8 RIXS plane data in the iron pre-edge and Kβ emission regions. The final state energy is the difference between incident and emission energies; highest and lowest emission intensities correspond to dark-red and dark-blue colours in the contour plots. Top (**1**) and bottom (**[1Hy]⁺**) panels show Kβ^{1,3} and Kβ′ (left) and Kβ^{2,5} (right) spectral regions in the region of the two pre-edge peaks (main K-edge rise along the diagonals to the right). Absolute intensities for the two complexes differ because of slight variations in sample concentration and X-ray beam intensity. Directions for CIE (constant incident energy) and CFE (constant final state energy) transects are indicated in the upper left panel.

(Table 4, Fig. 3B). Accordingly, analysis of the Kβ^{1,3} CIE and CFE spectra provided experimental estimates of the energy differences between the unoccupied Fed$_{z^2}$ (LUMO) and Fed$_{x^2-y^2}$ levels (mean of ~0.5 eV for **1** and ~0.9 eV for **[1Hy]⁺**), which are in reasonable agreement with the values from DFT (~0.4 eV and ~0.8 eV).

From CIE lines in the 1st pre-edge region for Kβ^{2,5} detection, the energies of valence-to-valence transitions can be estimated (Fig. 9B). Respective spectra in the final state energy region of about 4–19 eV for excitation at 7113.4 eV into Fed levels were well simulated using 5 Gaussians at similar energies within ±0.2 eV for **1** and **[1Hy]⁺**, except for the lowest energy maximum, which was at ~0.8 eV higher energy for **[1Hy]⁺** (Table 4). We note that the lowest energy maximum was insufficiently resolved for **1** because it overlaps with the elastic scattering peak of the incident X-rays. For excitation at 7115.8 eV preferentially into (CO)s,p levels (compare Fig. 3), the CIE spectra were shifted to about 2 eV higher final state energies and 3 maxima were discernable, which were at similar energies for **1** and **[1Hy]⁺** (Fig. S2,† Table 4).

At present, RIXS data in the Kβ region, *i.e.* for resonant excitation, cannot be calculated with the ORCA DFT-package. However, comparison of apparent CIE spectra derived from DFT-calculated Kβ^{2,5} lines for non-resonant excitation (Fig. 5) still was in quite good agreement with the experimental data, taking into account the limited spectral resolution of our experimental Kβ^{2,5} CIE spectra (Fig. 9B). This presumably means that the possibly small perturbations of the MO energy differences and valence-to-core emission yields in the Kβ^{2,5} region due to a surplus electron in the valence levels here were not resolved. Comparison of the metal and ligand contributions to the calculated Kβ^{2,5} emission maxima allows for approximate attributions of the CIE line features to Fe d→d, ligands,p→Fed, and (for excitation into *e.g.* (CO)s,p levels, Fig. S2†) ligands,p→ligands,p transitions (Fig. 7 and 9B). Accordingly, the mean energy differences between occupied and empty Fed levels (d→d transition) are estimated as ~2.9 eV for **1** and ~3.7 eV for **[1Hy]⁺** (Δ*E* = 0.8 eV) from the experimental CIE data, which is in reasonable agreement with the values of ~3.4 eV and ~4.1 eV (Δ*E* = 0.7 eV) from the

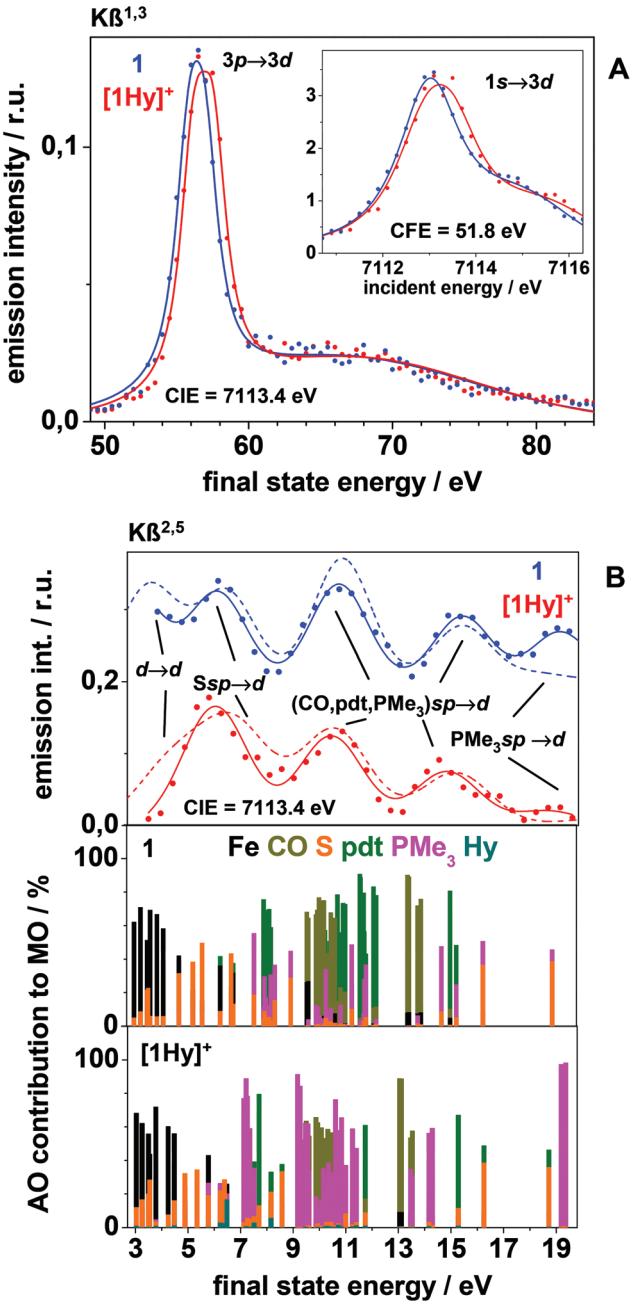

Fig. 9 Transects through Kβ RIXS planes and DFT calculations. (A) CIE and CFE (inset) line plots in the $K\beta^{1,3}$ emission region for resonant excitation (Fig. 8, left) and for the indicated energies; spectra were normalized to unity area. Curves represent fits to the data points with parameters in Table 4. (B) Top panel: CIE line plots in the $K\beta^{2,5}$ emission region for resonant excitation at 7113.4 eV (Fig. 8, right); spectra were normalized to unity area; the spectrum of **1** was vertically shifted. Dots, experimental data; solid lines, fits with 5 Gaussians and parameters in Table 4. Dashed lines show fits using the same spectral resolution as in the experiment (Table 4) to DFT-calculated $K\beta^{2,5}$ emission intensities for non-resonant excitation (see Fig. 5), displayed on a final state energy axis (calculated emission energies minus 7113.4 eV), which was multiplied by a factor of 1.25 for better comparison with the experimental data. Indicated transition assignments resulted from comparison of experimental emission peaks with contributions from iron or ligand AOs to the calculated emission peaks, as shown in the middle (**1**) and bottom (**[1Hy]$^+$**) panels. The bridging ligand without the S-atoms here is denoted pdt.

Table 4 Comparison of emission line energies from RIXS data and DFT calculations

	1		**[1Hy]$^+$**		**[1Hy]$^+$ − 1**	
	Final state energy, E [eV]				ΔE [eV]	
Spectrum	Exp.	DFT[d]	Exp.	DFT[d]	Exp.	DFT[d]
CIE $K\beta^{1,3}$ (7113.4 eV)	55.9	—	56.2	—	0.3	—
	56.7	—	57.6	—	0.9	—
	0.8[a]	—	1.4[a]	—	0.6[a]	—
CFE $K\beta^{1,3}$ (51.8 eV)	7112.9	—	7113.0	—	0.1	−0.1[b]
	7113.1	—	7113.5	—	0.4	0.3[b]
	0.2[a]	0.4[a,b]	0.5[a]	0.8[a,b]	0.3[a]	0.4[a,b]
CIE $K\beta^{2,5}$ (7113.4 eV)	2.9	3.4[c]	3.7	4.1[c]	0.8	0.7[c]
	5.4	5.7[c]	5.6	6.2[c]	0.2	0.5[c]
	9.4	9.8[c]	9.4	9.6[c]	0	−0.2[c]
	13.5	13.8[c]	13.3	13.5[c]	−0.2	−0.3[c]
	16.7	16.3[c]	16.6	16.1[c]	−0.1	−0.2[c]
	3.5[a]	3.2[a,c]	3.2[a]	3.0[a,c]	−0.2[a]	−0.2[a,c]
CIE $K\beta^{2,5}$ (7115.8 eV)	7.8	—	7.9	—	0.1	—
	11.1	—	11.0	—	−0.1	—
	15.6	—	15.3	—	−0.3	—
	3.9[a]	—	3.7[a]	—	−0.2[a]	—

CIE = constant incident energy, CFE = constant final state energy; respective energies are indicated). Experimental values were derived from Lorentzian fits of spectra in Fig. 9A for resonant excitation (FWHM of 0.6 eV for CFE $K\beta^{1,3}$ and 1.5 eV for CIE $K\beta^{1,3}$; an additional Gaussian at 7115.3 eV for CFE $K\beta^{1,3}$ and at 67.1 eV for CIE $K\beta^{1,3}$ was used) and Gaussian fits of spectra in Fig. 9B and S2 (FWHM = 2.3 eV). [a] Values are the (mean) differences between adjacent peak energies in the vertical direction of the table. [b] Values correspond to DFT-calculated transition energies for XAS pre-edge spectra (Fig. 3B) and represent the difference between the mean energies for Fe1 and Fe2 of the two Fed($x^2 - y^2$) transitions and the Fed(z^2) transition. [c] DFT-calculated values for $K\beta^{2,5}$ peaks are for non-resonant excitation and were obtained by Gaussian fits of respective spectra (Fig. 9B). [d] DFT values were obtained after applying a scaling factor of 1.25 to the respective calculated energy axes and realignment with the experimental spectra.

calculated CIE data (Fig. 9B) and of ~3.3 eV and ~3.8 eV (ΔE = 0.5 eV) from the calculated Fed-MO energies (Fig. 2).

The Fe d→d transition energies of about 2.5–4.0 eV correspond to photon wavelengths of 500–300 nm, *i.e.* in the green and near-UV region of the visible spectrum; all other transitions are in the UV at <225 nm. Thus, the optical (electronic) absorption spectrum of **[1Hy]$^+$** was expected to show a loss of intensity in this region compared to that of **1**, due to the shift of Fe d→d transitions to higher energies. Indeed, the UV/vis spectrum of **1** shows a prominent absorption maximum at ~350 nm and broad absorption around 500 nm, both of which are almost completely absent in the spectrum of **[1Hy]$^+$** (Fig. 10). Comparison of the (**[1Hy]$^+$ − 1**) UV/vis and $K\beta^{2,5}$ RIXS spectra allows for assignment of the absorption peak at ~350 nm and of the broader features to metal-to-metal charge transfer (MMCT) transitions (*i.e.* Fe d→d) in **1**, which are blue-shifted by >100 nm in **[1Hy]$^+$** (Fig. 9 and 10; Table 4). An absorption maximum at ~220 nm, which is present for **1** and increased for **[1Hy]$^+$**, is attributed to ligand-to-metal charge transfer (LMCT) mostly of Fed→Ss,p character in **1**, but may gain MMCT contributions in **[1Hy]$^+$** (Fig. 10).

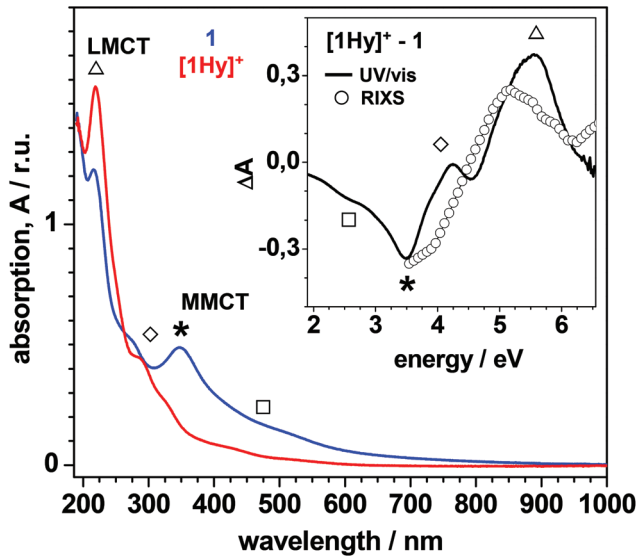

Fig. 10 UV/vis absorption spectra of complexes in acetonitrile solution. Spectra were normalized to concentrations of ~90 μM in MeCN. Inset: comparison of UV/vis and Kβ^{2,5} CIE (from RIXS data, scaled for comparison, see Fig. 9) difference spectra. Peak features marked by symbols are attributed to the LMCT or MMCT transitions as outlined in the text.

Discussion and conclusions

Binding of a bridging-hydride (Hy) to a symmetric diiron complex causes pronounced spectral changes of Fe pre-edge absorption spectra and Kβ emission spectra, highlighting the Hy influence on the electronic structure. The respective spectral alterations (energy shifts and intensity changes) were similar to those of a more asymmetric complex ([**2Hy**]$^+$ = [(μ-H)-(μ-adt)[Fe(CO)$_2$(PMe$_3$]$_2$]$^+$, adt = SCH$_2$(NCH$_2$Ph)H$_2$CS). [**2Hy**]$^+$ was derived by protonation of the parent compound (**2**) in MeCN solution, causing also formation of rotamers.[91] The specific Hy-induced spectral features for diiron models thus appear to be relatively insensitive to individual ligation patterns and geometries at the irons and any ligand reorientations upon solvation.[91]

This is rationalized by three prevailing effects: first, Hy-binding in both [**1Hy**]$^+$ and [**2Hy**]$^+$ [91] leaves the iron oxidation state practically unchanged and the weak hydride (H$^-$) character of the proton at the Fe–Fe bond is achieved by electron density transfer to Hy (and Fe) from the CO and PMe$_3$ ligands and the dithiolate bridge. For [**1Hy**]$^+$, prevailing donation from the S-pdt ligands has been discussed previously.[49,126] An Fe^{II}–H$^-$–Fe^{II} configuration in [**1Hy**]$^+$ *vs.* an Fe^I–Fe^I configuration in **1** has been suggested.[111] However, this view is challenged because the effective iron oxidation state in **1** and [**1Hy**]$^+$ appears to be invariant. Secondly, Hy-binding causes a symmetrization of the molecular structure, due to CO and PMe$_3$ ligand rearrangements and elongation of the Fe–Fe distance. This has been noted before for the PF$_6^-$ salt of [**1Hy**]$^+$ [49,111] and holds also for the isostructural BF$_4^-$ salt. Notably, **1** and [**1Hy**]$^+$ in the solid state adopt a basal-transoid geometry whereas in solution the apical–basal isomer of **1** may prevail,[111,127,128] depending on the solvent.[128–130] Thus, XAES spectral changes due to rotamer formation may be expected.[91] Concomitant symmetrization of the electronic configuration manifests, *e.g.*, in enhanced delocalization of Fed-dominated MOs over Fe1 and Fe2 and of (CO)s,p levels onto the Fe ions in [**1Hy**]$^+$ and [**2Hy**]$^+$. Finally, MOs with significant Hy character in particular contribute to the Kβ^{2,5} spectra and the reduced yield of the HOMO→1s decay reflects diminished Fed character of the HOMO (in [**2Hy**]$^+$)[91] or enhanced HOMO localization at Fe2 (in [**1Hy**]$^+$).

The complexes **1** and [**1Hy**]$^+$ have been extensively characterized in the literature using, *e.g.*, ^{1}H- or ^{2}H-NMR and FTIR,[49,56,111,126–132] but a detailed picture of their electronic structures had not been reported, partly because DFT calculation for example of vibrational spectra is a difficult task.[67,133] For a variety of iron complexes[84,91,100,106,107] and for **1** and [**1Hy**]$^+$, spectral features of pre-edge absorption and Kβ^{2,5} emission spectra were reproduced by DFT at the cost-efficient BP86/TZVP+P theory level. This has allowed experimental estimation of core-to-valence, valence-to-core, and valence-to-valence transition energies. An apparent underestimation of respective electronic energy differences was observed for this DFT approach, but a slight scaling of the calculated energy axes (by a factor of 1.25, see the next section) results in good agreement between the experimental and calculated energy values (see Tables 3 and 4).[84,91] This systematic deviation, however, does not affect the general conclusions drawn on the electronic structures.

The analysis of XAES-DFT data for **1** and [**1Hy**]$^+$ has revealed spin-pairing of the formal Fe^I(d^7)ions in low-spin states, provided energy differences between Fe3d- and (CO)s,p-dominated MOs of 1.6 eV and 2.1 eV (DFT: 1.3 eV and 1.8 eV, scaling by a factor of 1.25 yields 1.6 eV and 2.2 eV), a HOMO–LUMO gap (for **1**) of 3.0 ± 0.5 eV (DFT: 2.5 eV or scaled 3.1 eV), and energy separations of unoccupied Fed (x^2-y^2) and (z^2) levels of ~0.5 eV and ~0.9 eV (DFT: ~0.3 eV and ~0.6 eV or scaled ~0.4 eV and ~0.8 eV). This shows that the experimental and calculated (scaled) energy differences match within about ±0.1 eV. The estimated Fe d→d transition energies of 2.9–3.7 eV correspond to optical absorption features around 500–300 nm, which therefore are assigned to MMCT transitions. A prominent absorption peak at ~350 nm for **1** previously has been attributed to MLCT[128] and now is reassigned to MMCT mostly of Fe d→d character.

The XAES spectral features for **1** and [**1Hy**]$^+$ generally agree with correlations to structural properties for other low-spin iron compounds.[84,91] This corroborates that the decreasing Kβ^{2,5} emission intensity for longer Fe–ligand bonds is due to reduced electronic overlap of occupied and empty MOs.[84] A general trend emerges also for the HOMO, which is delocalized over both Fe ions for fully symmetric complexes (*e.g.* for [(OC)$_3$Fe(μ(CO))$_3$Fe(CO)$_3$)], largely located on one Fe ion for very asymmetric ligation (*e.g.* in **3** = [(CO)$_3$Fe(μ-bdtCl$_2$)Fe(CO)-(Ph$_2$PCH$_2$NCH$_3$CH$_2$PPh$_2$)], (bdt = benzene-1,2-dithiolate),[84] and slightly (for **1**) or more pronouncedly (for [**1Hy**]$^+$ and

$[\mathbf{2Hy}]^+$ [91]) localized at Fe2. The first reduction potential of $[\mathbf{1Hy}]^+$ is about 0.75 V more positive than that of **1**,[132] in line with the lower calculated LUMO energy and the correlation between the HOMO and LUMO energies and the first oxidation and reduction potentials for $[\mathbf{2Hy}]^+$ and **2**.[91] HOMO–LUMO gaps of ~2.5 eV for **1**, ~2.3 eV for **2**, and ~2.8 eV for **3**[84,91] were estimated from the Fe pre-edge and Kβ[2,5] energies and confirmed by DFT; for $[\mathbf{1Hy}]^+$ an ~0.1 eV decrease and for **2** an ~0.1 eV increase of the gap were observed. Apparently, the HOMO/LUMO energies are determined by the interplay between the electron donation and abstraction properties of the diverse terminal and bridging-dithiolate ligands. We show that qualitative assignment of electronic transitions for diiron compounds in Kβ RIXS data is feasible, even for the neglect of interactions between a resonantly excited surplus Fed (or, *e.g.*, (CO)s,p) electron and the other valence electrons in the current distribution of the ORCA DFT-package.[113]

Resonant excitation into (i) $\mathrm{Fed}_{z^2,x^2-y^2}$ or (ii) (CO)s,p levels probes exchange–coupling interactions between a spin-up (down) hole in the Fe 3p level and spin-up (down) Fed/ligands, p electrons in the $1s^2 3p^5 d/s,p^{n+1}$ final state.[79,80] Respective Kβ′ intensities were larger compared to those observed for non-resonant excitation, as explained by the surplus excited-level unpaired spin in the low-spin states, and similar to the intensities for iron reference compounds holding one unpaired spin (i) or lower (ii). Presumably, a decrease of the coupling strengths for the unpaired spin in a higher energy (*i.e.* ligands, p) level accounts for the latter effect. The Kβ′ emission thus seems to reflect the effective spin state. Along this line, compared to **1** for $[\mathbf{1Hy}]^+$ the effective spin count was slightly reduced for non-resonant excitation due to the enhanced l.s. $O_h Fe^{II}$ character in $[\mathbf{1Hy}]^+$. On the other hand, excitation into (CO)s,p or Fed levels resulted in slightly smaller or larger spin counts for $[\mathbf{1Hy}]^+$, compatible with the higher energies of (CO)s,p and lower energies of Fed levels in this complex. Depending on the energy of resonant excitation, even limited site-selectivity for preferential probing of Fe1 or Fe2 was observed. This may offer a way for experimental determination of electronic parameters of the individual iron sites.[84]

In summary, the experimentally determined energy differences allow for a comprehensive comparison of the changes of valence electronic levels in response to the Hy-binding in $[\mathbf{1Hy}]^+$ compared to **1** (Fig. 11). The extraction of electron density from the ligands by the Hy and Fe ions, *i.e.* the delocalization of the positive charge of the proton (H^+) at the Fe–Fe bond onto the ligands, causes even a slight reduction and enhanced O_h character of iron. This is reflected in overall elongated and thus more ionic Fe–ligand bonds and correlates with an energy increase by ~0.7 eV of ligands,p-dominated MOs. These results corroborate a previous Mössbauer study of (μ-dmpdt)$[Fe(CO)_2(PMe_3)]_2$ (dmpdt = $SCH_2CMe_2CH_2S$) (**4**) and its bridging-hydride derivative $[(\mu\text{-H})(\mu\text{-dmpdt})[Fe(CO)_2(PMe_3)]_2]^+$ ($[\mathbf{4Hy}]^+$), which are analogues of **1** and $[\mathbf{1Hy}]^+$.[112] The isomer shift for the irons of $[\mathbf{4Hy}]^+$, δ = 0.04 mms^{-1}, is similar to that for **4**, δ = 0.06 mms^{-1} and 0.07 mms^{-1}, *i.e.* electron density that converts H^+ into the bridging Hy is largely derived from the CO and phosphine ligands, without changing the electron density of the irons.[112] For the occupied MOs with $\mathrm{Fed}_{xy,yz,xz}$ character, an energy decrease by roughly −0.3 eV is attributed to decreased electron density in these orbitals, which point to the voids between the Fe–ligand bonds. On the other hand, increased electron density in the unoccupied $\mathrm{Fed}_{x^2-y^2}$ MOs directed along the Fe–ligand bonds accounts for their ~0.7 eV energy increase (Fig. 11). The Fed_{z^2} levels align with the Fe–Hy bonds and the bonds to the apical CO ligands and their almost unchanged energies are related to decreased electron density in these MOs, counteracted by the slight negative charge on Hy. In addition, the structural symmetrization causes an elongation of the Fe–Fe distance. Investigations on electronic structures in a larger series of iron–hydride complexes may be expected to unravel further relationships between the molecular and electronic configurations.

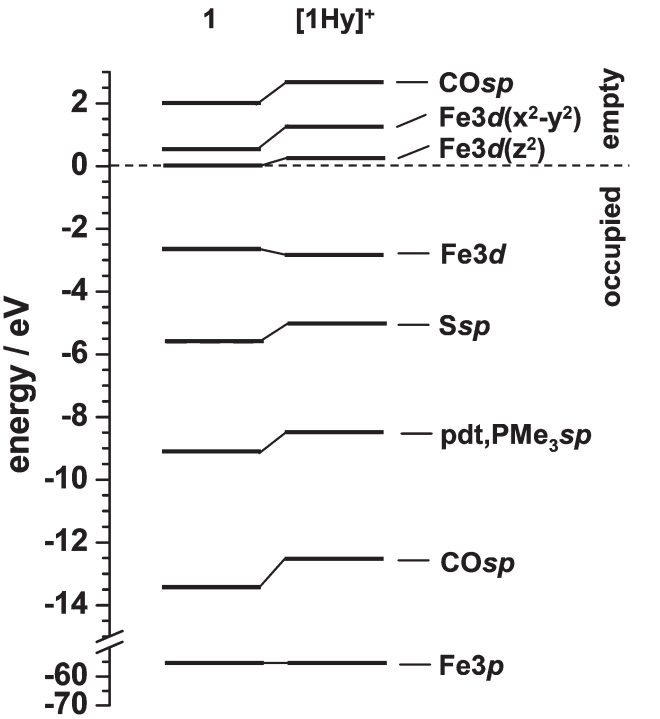

Fig. 11 Electronic energy levels of valence states. Given energies resulted from a combination of transition energies determined from XAS, XES, and RIXS data (Tables 3 and 4) and represented the mean respective values. The energy of the LUMO with predominant $\mathrm{Fed}(z^2)$ character for **1** was arbitrarily chosen as the zero energy level and data for $[\mathbf{1Hy}]^+$ were normalized by application of the same energy shift, which accounts for the same Fe3p-level energy for both complexes. The labels denote the dominant Fe- or ligand-AO character of respective MOs.

In conclusion, the influence of a bridging hydride on the electronic structure of [FeFe] model complexes is well revealed by XAES-DFT. The feasibility of discrimination between the effects of terminally coordinated and bridging hydride species is less clear. For the [FeFe] hydrogenases, it is an open question whether and in which intermediate bridging and/or terminal hydride species at the diiron site are involved in the reaction cycle. Future XAES studies including site-selective

approaches[84,91–93] may enable monitoring of hydride intermediates also in the [FeFe] hydrogenases, thereby allowing for deeper insight into their H_2-formation mechanism.

Abbreviations

AO	Atomic orbital
DFT	Density functional theory
EXAFS	Extended X-ray absorption fine structure
FWHM	Full width at half maximum
HOMO	Highest occupied MO
Hy	Hydride
L/MCT	Ligand/metal charge transfer
LUMO	Lowest unoccupied MO
MO	Molecular orbital
RIXS	Resonant inelastic X-ray scattering
XANES	X-ray absorption near edge structure
XAS	X-ray absorption spectroscopy
XAES	X-ray absorption spectroscopy using narrow-band emission detection
XES	X-ray emission spectroscopy

Acknowledgements

Financial support from the Deutsche Forschungsgemeinschaft (DFG; grants Ha3265/3-1 and Ha3265/6-1 and funding within the Unicat Cluster of Excellence Berlin to M. H.) and the United States National Science Foundation and the R. A. Welch Foundation (grants CHE-0910679 and A-0924 to M. Y. D.) is gratefully acknowledged. K. G. V. H. thanks "Stiftelsen Bengt Lundqvist minne" and the Wenner-Gren Foundation for fellowships. M. H. thanks the DFG for a Heisenberg fellowship. We thank Drs T.-C. Weng, K. Kvashnina, and P. Glatzel at beamline ID26 for excellent technical support and the ESRF for granting of a Long Term Project (SC3218, to M. H.).

References

1 K. Yvon and G. Renaudin, in *Encyclopedia of Inorganic Chemistry*, ed. R. B. King, Wiley, Chichester, 2005, vol. 3, pp. 1814–1846.
2 *Metal ions in Biology*, ed. A. Sigel and H. Sigel, Taylor & Francis, New York, 2005, vol. 39.
3 Z. D. Nagel and J. P. Klinman, *Chem. Rev.*, 2006, **106**, 3095–3118.
4 *Hydrogen as a Fuel: Learning from Nature*, ed. R. F. Cammack and R. Robson, Taylor & Francis, London, UK, 1997.
5 R. Bau, R. G. Teller, S. W. Kirtley and T. F. Koetzle, *Acc. Chem. Res.*, 1979, **12**, 176–183.
6 G. J. Kubas, *Metal Dihydrogen and -Bond Complexes – Structure, Theory, and Reactivity*, Kluwer Academic Publishers, New York, 2001.
7 G. S. McGrady and G. Guilera, *Chem. Soc. Rev.*, 2003, **32**, 383–392.
8 S. F. Parker, *Coord. Chem. Rev.*, 2010, **254**, 215–234.
9 M. P. Suh, H. J. Park, T. K. Prasad and D. W. Lim, *Chem. Rev.*, 2012, **112**, 782–835.
10 B. Sakintuna, F. Lamari-Darkrim and M. Hirscher, *Int. J. Hydrogen Energy*, 2007, **32**, 1121–1140.
11 R. R. Davda, J. W. Shabaker, G. W. Huber, R. D. Cortright and J. A. Dumesic, *Appl. Catal., B*, 2005, **56**, 171–186.
12 N. Armaroli and V. Balzani, *ChemSusChem*, 2011, **4**, 21–36.
13 T. Abbasi and S. A. Abbasi, *Renew. Sustain. Energy Rev.*, 2011, **15**, 3034–3040.
14 *Experts Workshop on Metal Hydrides in Biology*, ed. F. S. Armstrong, http://metalhydride.org/Meeting-Information/, Oxford, UK, 2012.
15 R. K. Thauer, A. K. Kaster, M. Goenrich, M. Schick, T. Hiromoto and S. Shima, *Annu. Rev. Biochem.*, 2010, **79**, 507–536.
16 D. W. Mulder, E. M. Shepard, J. E. Meuser, N. Joshi, P. W. King, M. C. Posewitz, J. B. Broderick and J. W. Peters, *Structure*, 2011, **19**, 1038–1052.
17 A. Parkin and F. Sargent, *Curr. Opin. Chem. Biol.*, 2012, **16**, 26–34.
18 F. A. Armstrong and J. C. Fontecilla-Camps, *Science*, 2008, **321**, 498–499.
19 S. T. Stripp and T. Happe, *Dalton Trans.*, 2009, 9960–9969.
20 D. W. Mulder, E. M. Shepard, J. E. Meuser, N. Joshi, P. W. King, M. C. Posewitz, J. B. Broderick and J. W. Peters, *Structure*, 2011, **19**, 1038–1052.
21 C. Madden, M. D. Vaughn, I. Diez-Perez, K. A. Brown, P. W. King, D. Gust, A. L. Moore and T. A. Moore, *J. Am. Chem. Soc.*, 2012, **134**, 1577–1582.
22 J. W. Peters, W. N. Lanzilotta, B. J. Lemon and L. C. Seefeldt, *Science*, 1998, **282**, 1853–1858.
23 Y. Nicolet, B. J. Lemon, J. C. Fontecilla-Camps and J. W. Peters, *Trends Biochem. Sci.*, 2000, **25**, 138–143.
24 W. Roseboom, A. L. De Lacey, V. M. Fernandez, E. C. Hatchikian and S. P. Albracht, *J. Biol. Inorg. Chem.*, 2006, **11**, 102–118.
25 A. Silakov, C. Kamp, E. Reijerse, T. Happe and W. Lubitz, *Biochemistry*, 2009, **48**, 7780–7786.
26 A. Silakov, B. Wenk, E. Reijerse and W. Lubitz, *Phys. Chem. Chem. Phys.*, 2009, **11**, 6592–6599.
27 O. F. Erdem, L. Schwartz, M. Stein, A. Silakov, S. Kaur-Ghumaan, P. Huang, S. Ott, E. J. Reijerse and W. Lubitz, *Angew. Chem., Int. Ed.*, 2011, **50**, 1439–1443.
28 S. T. Stripp, G. Goldet, C. Brandmayr, O. Sanganas, K. A. Vincent, M. Haumann, F. A. Armstrong and T. Happe, *Proc. Natl. Acad. Sci. U. S. A.*, 2009, **106**, 17331–17336.
29 C. Lambertz, N. Leidel, K. G. Havelius, J. Noth, P. Chernev, M. Winkler, T. Happe and M. Haumann, *J. Biol. Chem.*, 2011, **286**, 40614–40623.
30 M. K. Bruska, M. T. Stiebritz and M. Reiher, *J. Am. Chem. Soc.*, 2011, **133**, 20588–20603.

31 P. Knörzer, A. Silakov, C. E. Foster, F. A. Armstrong, W. Lubitz and T. Happe, *J. Biol. Chem.*, 2012, **287**, 1489–1499.
32 J. M. Kuchenreuther, C. S. Grady-Smith, A. S. Bingham, S. J. George, S. P. Cramer and J. R. Swartz, *PLoS One*, 2010, **5**, e15491.
33 T. Zhou, Y. Mo, A. Liu, Z. Zhou and K. R. Tsai, *Inorg. Chem.*, 2004, **43**, 923–930.
34 P. E. Siegbahn, J. W. Tye and M. B. Hall, *Chem. Rev.*, 2007, **107**, 4414–4435.
35 A. S. Adamska, A. Silakov, C. Lambertz, O. Rüdiger, T. Happe, E. Reijerse and W. Lubitz, *Angew. Chem., Int. Ed.*, 2012, **51**, 14458–14562.
36 M. Y. Darensbourg, *Nature*, 2005, **433**, 589–591.
37 M. Y. Darensbourg, *Commun. Inorg. Chem.*, 2010, **31**, 144–152.
38 M. Y. Darensbourg, E. J. Lyon and J. J. Smee, *Coord. Chem. Rev.*, 2000, **206**, 533–561.
39 M. Y. Darensbourg and R. D. Bethel, *Nat. Chem.*, 2012, **4**, 11–13.
40 F. Gloaguen and T. B. Rauchfuss, *Chem. Soc. Rev.*, 2009, **38**, 100–108.
41 T. B. Rauchfuss, *Science*, 2007, **316**, 553–554.
42 C. Tard and C. J. Pickett, *Chem. Rev.*, 2009, **109**, 2245–2274.
43 C. Tard, X. Liu, S. K. Ibrahim, M. Bruschi, L. De Gioia, S. C. Davies, X. Yang, L. S. Wang, G. Sawers and C. J. Pickett, *Nature*, 2005, **433**, 610–613.
44 F. Gloaguen, J. D. Lawrence, T. B. Rauchfuss, M. Benard and M. M. Rohmer, *Inorg. Chem.*, 2002, **41**, 6573–6582.
45 J. M. Camara and T. B. Rauchfuss, *Nat. Chem.*, 2012, **4**, 26–30.
46 D. J. Evans and C. J. Pickett, *Chem. Soc. Rev.*, 2003, **32**, 268–275.
47 M. T. Olsen, T. B. Rauchfuss and S. R. Wilson, *J. Am. Chem. Soc.*, 2010, **132**, 17733–17740.
48 X. Zhao, Y. M. Hsiao, C. H. Lai, J. H. Reibenspies and M. Y. Darensbourg, *Inorg. Chem.*, 2002, **41**, 699–708.
49 X. Zhao, I. P. Georgakaki, M. L. Miller, R. Mejia-Rodriguez, C. Y. Chiang and M. Y. Darensbourg, *Inorg. Chem.*, 2002, **41**, 3917–3928.
50 S. L. Matthews and D. M. Heinekey, *Inorg. Chem.*, 2010, **49**, 9746–9748.
51 G. Eilers, L. Schwartz, M. Stein, G. Zampella, L. de Gioia, S. Ott and R. Lomoth, *Chemistry*, 2007, **13**, 7075–7084.
52 S. Ezzaher, J. F. Capon, F. Gloaguen, F. Y. Petillon, P. Schollhammer, J. Talarmin, R. Pichon and N. Kervarec, *Inorg. Chem.*, 2007, **46**, 3426–3428.
53 M. H. Cheah, S. J. Borg and S. P. Best, *Inorg. Chem.*, 2007, **46**, 1741–1750.
54 M. T. Olsen, B. E. Barton and T. B. Rauchfuss, *Inorg. Chem.*, 2009, **48**, 7507–7509.
55 B. E. Barton and T. B. Rauchfuss, *Inorg. Chem.*, 2008, **47**, 2261–2263.
56 J. A. Wright, L. Webster, A. Jablonskyte, P. M. Woi, S. K. Ibrahim and C. J. Pickett, *Faraday Discuss.*, 2011, **148**, 359–371.
57 B. E. Barton and T. B. Rauchfuss, *J. Am. Chem. Soc.*, 2010, **132**, 14877–14885.
58 B. E. Barton, G. Zampella, A. K. Justice, L. De Gioia, T. B. Rauchfuss and S. R. Wilson, *Dalton Trans.*, 2010, **39**, 3011–3019.
59 N. Wang, M. Wang, J. Liu, K. Jin, L. Chen and L. Sun, *Inorg. Chem.*, 2009, **48**, 11551–11558.
60 M. H. Chiang, Y. C. Liu, S. T. Yang and G. H. Lee, *Inorg. Chem.*, 2009, **48**, 7604–7612.
61 L. Schwartz, G. Eilers, L. Eriksson, A. Gogoll, R. Lomoth and S. Ott, *Chem. Commun.*, 2006, 520–522.
62 J. I. van der Vlugt, T. B. Rauchfuss, C. M. Whaley and S. R. Wilson, *J. Am. Chem. Soc.*, 2005, **127**, 16012–16013.
63 X. Zhao, C.-Y. Chiang, M. L. Miller, M. V. Rampersad and M. Y. Darensbourg, *J. Am. Chem. Soc.*, 2003, **125**, 518–524.
64 P. I. Volkers and T. B. Rauchfuss, *J. Inorg. Biochem.*, 2007, **101**, 1748–1751.
65 S. Ezzaher, A. Gogoll, C. Bruhn and S. Ott, *Chem. Commun.*, 2010, **46**, 5775–5777.
66 T. J. Stewart, *Neutron and x-ray crystallographic studies on metal hydride complexes and organic ring inversion*, ProQuest, Ann Arbor, 2009.
67 L. Andrews, *Chem. Soc. Rev.*, 2004, **33**, 123–132.
68 P. J. Farmer and F. Sulc, *J. Inorg. Biochem.*, 2005, **99**, 166–184.
69 B. D. Dunlap, G. K. Shenoy, J. M. Friedt, P. J. Viccaro, D. Niarchos, H. Kierstead, A. T. Aldred and D. G. Westlake, *J. Appl. Phys.*, 1979, **50**, 7682–7686.
70 P. A. Bennett and J. C. Fuggle, *Phys. Rev. B: Condens. Matter*, 1982, **26**, 6030–6039.
71 J. H. Weaver, D. T. Peterson and R. L. Benbow, *Phys. Rev. B: Condens. Matter*, 1979, **20**, 5301–5312.
72 B. F. G. Johnson and J. S. McIndoe, *Coord. Chem. Rev.*, 2000, **200**, 901–932.
73 *Electron Paramagnetic Resonance*, ed. B. C. Gilbert and V. Chechik, Royal Society of Chemistry, London, 2000, vol. 23.
74 T. Shima, Y. Luo, T. Stewart, R. Bau, G. J. McIntyre, S. A. Mason and Z. Hou, *Nat. Chem.*, 2011, **3**, 814–820.
75 M. G. I. Galinato, C. M. Whaley, D. Roberts, P. Wang and N. Lehnert, *Eur. J. Inorg. Chem.*, 2011, 1147–1154.
76 V. Pelmenschikov, Y. Guo, H. Wang, S. P. Cramer and D. A. Case, *Faraday Discuss.*, 2011, **148**, 409–420.
77 C. J. Stromberg, C. L. Kohnhorst, G. A. Van Meter, E. A. Rakowski, B. C. Caplins, T. A. Gutowski, J. L. Mehalko and E. J. Heilweil, *Vib. Spectrosc.*, 2011, **56**, 219–227.
78 H. S. W. Shafaat, K. Weber, T. Petrenko, F. Neese and W. Lubitz, *Inorg. Chem.*, 2012, **51**, 11787–11797.
79 P. Glatzel and U. Bergmann, *Coord. Chem. Rev.*, 2005, **249**, 65–95.
80 F. De Groot and A. Kotani, *Core Level Spectroscopy of Solids*, Taylor & Francis CRC press, Boca Raton, FL, USA, 2008.
81 F. de Groot, *Chem. Rev.*, 2001, **101**, 1779–1808.

82 H. Dau and M. Haumann, *Coord. Chem. Rev.*, 2008, **252**, 273–295.
83 R. W. Strange and M. C. Feiters, *Curr. Opin. Struct. Biol.*, 2008, **18**, 609–616.
84 N. Leidel, P. Chernev, K. G. Havelius, S. Ezzaher, S. Ott and M. Haumann, *Inorg. Chem.*, 2012, 4546–4559.
85 U. Bergmann, P. Glatzel, J. H. Robblee, J. Messinger, C. Fernandez, R. Cinco, H. Visser, K. McFarlane, E. Bellacchio, S. Pizarro, K. Sauer, V. K. Yachandra, M. P. Klein, B. L. Cox, K. H. Nealson and S. P. Cramer, *J. Synchrotron Radiat.*, 2001, **8**, 199–203.
86 H. Namatame, A. Fujimori, H. Takagi, S. Uchida, F. M. de Groot and J. C. Fuggle, *Phys. Rev. B: Condens. Matter*, 1993, **48**, 16917–16925.
87 M. Abbate, J. C. Fuggle, A. Fujimori, L. H. Tjeng, C. T. Chen, R. Potze, G. A. Sawatzky, H. Eisaki and S. Uchida, *Phys. Rev. B: Condens. Matter*, 1993, **47**, 16124–16130.
88 M. Grioni, J. F. van Acker, M. T. Czyzyk and J. C. Fuggle, *Phys. Rev. B: Condens. Matter*, 1992, **45**, 3309–3318.
89 P. J. Weijs, H. van Leuken, R. A. de Groot, J. C. Fuggle, S. Reiter, G. Wiech and K. H. Buschow, *Phys. Rev. B: Condens. Matter*, 1991, **44**, 8195–8203.
90 F. M. de Groot, J. C. Fuggle, B. T. Thole and G. A. Sawatzky, *Phys. Rev. B: Condens. Matter*, 1990, **42**, 5459–5468.
91 N. Leidel, P. Chernev, K. G. Havelius, L. Schwartz, S. Ott and M. Haumann, *J. Am. Chem. Soc.*, 2012, **134**, 14142–14157.
92 O. Sanganas, S. Löscher, S. Pfirrmann, M. Marinos, P. Glatzel, T.-C. Weng, C. Limberg, M. Driess, H. Dau and M. Haumann, *J. Phys. Conf. Ser.*, 2009, **190**, 012199, 1–4.
93 P. Glatzel, L. Jacquamet, U. Bergmann, F. M. F. de Groot and S. P. Cramer, *Inorg. Chem.*, 2002, **41**, 3121–3127.
94 H. Yamaoka, M. Oura, M. Taguchi, T. Morikawa, K. Takahiro, A. Terai, K. Kawatsura, A. M. Vlaicu, Y. Ito and T. Mukoyama, *J. Phys. Soc. Jpn.*, 2004, **73**, 3182–3191.
95 J. Badro, V. V. Struzhkin, J. F. Shu, R. J. Hemley, H. K. Mao, C. C. Kao, J. P. Rueff and G. Y. Shen, *Phys. Rev. Lett.*, 1999, **83**, 4101–4104.
96 F. M. F. Degroot, A. Fontaine, C. C. Kao and M. Krisch, *J. Phys.: Condens. Matter*, 1994, **6**, 6875–6884.
97 G. Peng, X. Wang, C. R. Randall, J. A. Moore and S. P. Cramer, *Appl. Phys. Lett.*, 1994, **65**, 2527–2529.
98 G. Peng, F. M. F. Degroot, K. Hamalainen, J. A. Moore, X. Wang, M. M. Grush, J. B. Hastings, D. P. Siddons, W. H. Armstrong, O. C. Mullins and S. P. Cramer, *J. Am. Chem. Soc.*, 1994, **116**, 2914–2920.
99 I. Zaharieva, P. Chernev, M. Risch, L. Gerencser, G. Berggren, G. Shevchenko, M. Anderlund, T.-C. Weng, M. Haumann and H. Dau, *J. Phys. Conf. Ser.*, 2009, **190**, 012142, 1–6.
100 N. Lee, T. Petrenko, U. Bergmann, F. Neese and S. DeBeer, *J. Am. Chem. Soc.*, 2010, **132**, 9715–9727.
101 P. Chandrasekaran, S. C. E. Stieber, T. J. Collins, L. Que, F. Neese and S. DeBeer, *Dalton Trans.*, 2011, **40**, 11070–11079.
102 S. D. George, T. Petrenko and F. Neese, *J. Phys. Chem. A*, 2008, **112**, 12936–12943.
103 S. D. George, J. F. Berry, N. Aliaga-Alcalde, T. Petrenko, E. Bill, B. Mienert, W. Sturhahn, K. Wieghardt and F. Neese, *Abstr. Pap. Am. Chem. Soc.*, 2007, **233**, 455.
104 N. Leidel, A. Popovic-Bijelic, K. G. Havelius, P. Chernev, N. Voevodskaya, A. Gräslund and M. Haumann, *Biochim. Biophys. Acta*, 2012, **1817**, 430–444.
105 F. M. de Groot, P. Glatzel, U. Bergmann, P. A. van Aken, R. A. Barrea, S. Klemme, M. Havecker, A. Knop-Gericke, W. M. Heijboer and B. M. Weckhuysen, *J. Phys. Chem. B*, 2005, **109**, 20751–20762.
106 C. J. Pollock and S. DeBeer, *J. Am. Chem. Soc.*, 2011, **133**, 5594–5601.
107 K. M. Lancaster, K. D. Finkelstein and S. DeBeer, *Inorg. Chem.*, 2011, **50**, 6767–6774.
108 K. M. Lancaster, M. Roemelt, P. Ettenhuber, Y. Hu, M. W. Ribbe, F. Neese, U. Bergmann and S. DeBeer, *Science*, 2011, **334**, 974–977.
109 M. U. Delgado-Jaime, B. R. Dible, K. P. Chiang, W. W. Brennessel, U. Bergmann, P. L. Holland and S. DeBeer, *Inorg. Chem.*, 2011, **50**, 10709–10717.
110 E. Gallo, C. Lamberti and P. Glatzel, *Phys. Chem. Chem. Phys.*, 2011, **13**, 19409–19419.
111 X. Zhao, I. P. Georgakaki, M. L. Miller, J. C. Yarbrough and M. Y. Darensbourg, *J. Am. Chem. Soc.*, 2001, **123**, 9710–9711.
112 C.-H. Hsieh, O. F. Erdem, S. D. Harman, M. L. Singleton, E. Reijerse, W. Lubitz, C. V. Popescu, J. H. Reibenspiess, S. M. Brothers, M. B. Hall and M. Y. Darensbourg, *J. Am. Chem. Soc.*, 2012, **134**, 13089–13101.
113 F. Neese. *ORCA: An ab initio, DFT, and semiempirical electronic structure package, V. 2.6.35, Theoretical Chemistry Group*, Max Planck Institute for Chemical Energy Conversion, Mülheim, Germany, 2012.
114 A. D. Becke, *Phys. Rev. A*, 1988, **38**, 3098–3100.
115 J. P. Perdew, *Phys. Rev. B: Condens. Matter*, 1986, **33**, 8822–8824.
116 K. Kim and K. D. Jordan, *J. Phys. Chem.*, 1994, **98**, 10089–10094.
117 A. Schäfer, C. Huber and R. Ahlrichs, *J. Chem. Phys.*, 1994, **100**, 5829–5835.
118 R. S. Mulliken, *J. Chem. Phys.*, 1955, **23**, 1833–1840.
119 T. E. Westre, P. Kennepohl, J. G. DeWitt, B. Hedman, K. O. Hodgson and E. I. Solomon, *J. Am. Chem. Soc.*, 1997, **119**, 6297–6314.
120 K. Sakurai, H. Eba, C. Numako and J. Iihara, *Anal. Chem.*, 2000, **72**, 2613–2617.
121 P. Glatzel, U. Bergmann, F. M. F. de Groot and S. P. Cramer, *Phys. Rev. B: Condens. Matter*, 2001, 64.
122 K. Hamalainen, C. C. Kao, J. B. Hastings, D. P. Siddons, L. E. Berman, V. Stojanoff and S. P. Cramer, *Phys. Rev. B: Condens. Matter*, 1992, **46**, 14274–14277.
123 K. Tsutsumi, H. Nakamori and K. Ichikawa, *Phys. Rev. B: Condens. Matter*, 1976, **13**, 929–933.
124 H. Hayashi, *Anal. Sci.*, 2008, **24**, 15–23.

125 G. Kaindl, W. D. Brewer, G. Kalkowski and F. Holtzberg, *Phys. Rev. Lett.*, 1983, **51**, 2056–2059.
126 T. Liu, B. Li, M. L. Singleton, M. B. Hall and M. Y. Darensbourg, *J. Am. Chem. Soc.*, 2009, **131**, 8296–8307.
127 P. W. Frederix, R. Kania, J. A. Wright, D. A. Lamprou, R. V. Ulijn, C. J. Pickett and N. T. Hunt, *Dalton Trans.*, 2012, 13112–13119.
128 J. A. Wright and C. J. Pickett, *Chem. Commun.*, 2009, 5719–5721.
129 R. Kania, P. W. Frederix, J. A. Wright, R. V. Ulijn, C. J. Pickett and N. T. Hunt, *J. Chem. Phys.*, 2012, **136**, 044521.
130 S. Kaziannis, S. Santabarbara, J. A. Wright, G. M. Greetham, M. Towrie, A. W. Parker, C. J. Pickett and N. T. Hunt, *J. Phys. Chem. B*, 2010, **114**, 15370–15379.
131 A. Jablonskyte, J. A. Wright and C. J. Pickett, *Dalton Trans.*, 2010, **39**, 3026–3034.
132 R. Mejia-Rodriguez, D. Chong, J. H. Reibenspies, M. P. Soriaga and M. Y. Darensbourg, *J. Am. Chem. Soc.*, 2004, **126**, 12004–12014.
133 M. Petkovic, *Spectrochim. Acta, Part A*, 2010, **77**, 942–947.
134 A. S. Pandey, T. V. Harris, L. J. Giles, J. W. Peters and R. K. Szilagyi, *J. Am. Chem. Soc.*, 2008, **130**, 4533–4540.